Mineralogical Magazine (2023), **87**, 789–806
doi:10.1180/mgm.2023.66

Article

Structure and thermal expansion of end-member olivines I: Crystal and magnetic structure, thermal expansion, and spontaneous magnetostriction of synthetic fayalite, Fe_2SiO_4, determined by high-resolution neutron powder diffraction

Evangelia K. Tripoliti[1,2], David P. Dobson[1], A. Dominic Fortes[1,3], Andrew R. Thomson[1,2], Paul F. Schofield[2] and Ian G. Wood[1]

[1]Dept. of Earth Sciences, University College London, Gower Street, London, WC1E 6BT, UK; [2]Dept. of Earth Sciences, The Natural History Museum, London, SW7 5BD, UK; and [3]ISIS Neutron and Muon Spallation Source, Rutherford Appleton Laboratory, Harwell Science and Innovation Campus, Chilton, Oxfordshire, OX11 0QX, UK

Abstract

The lattice parameters and the crystal and magnetic structures of Fe_2SiO_4 have been determined from 10 K to 1453 K by high-resolution time-of-flight neutron powder diffraction. Fe_2SiO_4 undergoes two antiferromagnetic phase transformations on cooling from room temperature: the first, at 65.4 K, is to a collinear antiferromagnet with moments on two symmetry-independent Fe ions; the second transition, at ~23 K, is to a structure in which the moments on one of the sets of Fe ions (those on the 'M1 site') become canted. The magnetic unit cell is identical to the crystallographic (chemical) unit cell and the space group remains *Pbnm* throughout. The magnetic structures have been refined and the results found to be in good agreement with previous studies; however, we have determined the spontaneous magnetostrictive strains, which have not been reported previously. In the paramagnetic phase of Fe_2SiO_4, at temperatures of 70 K and above, we find that the temperature dependence of the linear thermal expansion coefficient of the *b* axis takes an unusual form. In contrast to the behaviour of the expansion coefficients of the unit-cell volume and of the *a* and *c* axes, which show the expected reduction in magnitude below ~300 K, that of the *b* axis remains almost constant between ~70 K and 1000 K.

Keywords: fayalite; olivine; thermal expansion; magnetism; crystal structure

(Received 28 April 2023; accepted 15 August 2023; Accepted Manuscript published online: 25 August 2023; Associate Editor: Sergey V Krivovichev)

Introduction

The thermoelastic and thermodynamic properties of the olivine group of minerals are of considerable interest, being necessary to understand the structure of the Earth's upper mantle (down to 410 km depth), where olivine is believed to account for between 30% to 60% (by volume) for typical mantle phase assemblages (e.g. Ringwood, 1969; Bass and Anderson, 1984). Olivines with compositions between forsterite (Mg_2SiO_4) and fayalite (Fe_2SiO_4) are among the most studied minerals due to their abundance and importance in a spectrum of geological and cosmic environments, their physical properties determining, amongst other things, the formation and thermal evolution of planetary bodies. For example, as pointed out recently by Béjina *et al.* (2021), determination of the thermoelastic properties of iron-rich olivine is likely to be crucial in understanding the Martian interior. Since the original determination of their crystal structures by Bragg and Brown (1926), there have been numerous investigations of the temperature dependence of the volume of the $(Mg,Fe)_2SiO_4$ olivines. The first studies of the linear thermal expansion of olivines were made by Kozu *et al.* (1934) and Rigby *et al.* (1946) using dilatometers for their measurements. The first thermal expansion study for pure forsterite was made by Skinner (1962) using powder X-ray diffraction, and for pure fayalite by Suzuki *et al.* (1981), using dilatometry.

In the Mg–Fe solid-solution, the Fe^{2+} and Mg^{2+} ions are sufficiently similar in size that this substitution results in very little structural change (e.g. Hazen, 1977). However, the fayalite end-member does show some very significant differences in behaviour compared to that of the isostructural forsterite. In particular, fayalite becomes magnetically ordered at low temperature and the change with temperature in the thermal expansion coefficient of its *b* axis takes a very different form to that of forsterite. Fayalite is orthorhombic, with space group *Pbnm* and cell parameters $a \approx 4.82$ Å, $b \approx 10.48$ Å and $c \approx 6.09$ Å at room temperature. The crystal structure can be considered in terms of a layered hexagonal close-packed (HCP) oxygen network. Silicon ions occupy tetrahedral sites (in 4c positions at *x*, *y*, ¼, with $x \approx 0.43$ and

Corresponding author: Ian G. Wood; Email: ian.wood@ucl.ac.uk
Cite this article: Tripoliti E.K., Dobson D.P., Fortes A.D., Thomson A.R., Schofield P.F. and Wood I.G. (2023) Structure and thermal expansion of end-member olivines I: Crystal and magnetic structure, thermal expansion, and spontaneous magnetostriction of synthetic fayalite, Fe_2SiO_4, determined by high-resolution neutron powder diffraction. *Mineralogical Magazine* **87**, 789–806. https://doi.org/10.1180/mgm.2023.66

© The Author(s), 2023. Published by Cambridge University Press on behalf of The Mineralogical Society of the United Kingdom and Ireland. This is an Open Access article, distributed under the terms of the Creative Commons Attribution licence (http://creativecommons.org/licenses/by/4.0/), which permits unrestricted re-use, distribution and reproduction, provided the original article is properly cited.

$y \approx 0.10$ at room temperature) lying on mirror planes. Iron cations occupy two symmetrically non-equivalent octahedral sites, namely M1 (= Fe1) and M2 (= Fe2); the first of these is located in the 4a (0, 0, 0) positions and the second in 4c positions with $x \approx 0.99$ and $y \approx 0.28$ (Fig. 1). There are three non-symmetry-equivalent oxygen ions in the unit cell; two of these, O1 and O2, are located in 4c positions on the mirror planes, with $x \approx 0.77$, $y \approx 0.09$ and $x \approx 0.21$, $y \approx 0.45$, respectively, at room temperature. The remaining oxygen ions are in the general 8d positions, with $x \approx 0.29$, $y \approx 0.17$ and $z \approx 0.46$. The smaller, more distorted, M1 octahedral site (at 0, 0, 0) is located on a centre of symmetry, and shares edges with the larger M2 octahedral site – which lies on the mirror planes running perpendicular to the *c* axis, cutting it at ¼ and ¾. The coordination polyhedron of the M1 site is formed by bonding to two O1, two O2 and two O3 atoms; that for the M2 site involves bonding to one O1, one O2 and four O3 atoms. In the SiO_4 tetrahedra the Si bonds to one O1, one O2 and two O3 atoms.

Kondo and Miyahara (1963) were the first to propose that pure fayalite exhibits a Néel point between 77 and 300 K, however Santoro *et al.* (1966) were the first to report detailed information about the two magnetic transitions at 23 K and 65 K by means of neutron powder diffraction. Below 65 K the Fe_2SiO_4 structure is antiferromagnetically ordered (henceforth termed AFM1) with the spins of the Fe atoms on both the M1 and M2 sites having a collinear arrangement parallel to the *c* axis. Below 23 K, there is a different antiferromagnetic structure (AFM2) in which the spins on the Fe atoms at the M1 sites become canted, possessing components along all three crystallographic directions (e.g. Müller *et al.*, 1982). Suzuki *et al.* (1981) first identified the high-temperature anomalous behaviour of fayalite's *b* axis, which is completely different from that found in forsterite, with the thermal expansion coefficient for this axis showing a shallow, roughly parabolic form between 300 K and 1100 K, which they considered to be similar to the behaviour of some of the elastic moduli as reported by Sumino (1979). In subsequent studies, Kroll *et al.* (2012, 2014), also detected the anomalous behaviour of *b*, however their data are sparse below room temperatures and show significantly more scatter than those of Suzuki *et al.* (1981); furthermore, the behaviour of the thermal expansion coefficient of the *b* axis below room temperature reported by Kroll *et al.* (2014; as shown in figure 5b of their paper) differs markedly from that which we observe in the present study. Anomalous thermal expansion associated with a magnetic phase transition has also been reported by Sazonov *et al.* (2010) in the isostructural compound Co_2SiO_4. This material, however, differs markedly from Fe_2SiO_4; firstly, in that only one phase transition is observed, to the phase denoted here as AFM2 (at 50 K) and, secondly, as the *b* axis of Co_2SiO_4 (equivalent to the *a* axis in the *Pnma* setting of the space group used by Sazonov *et al.*, 2010) does not show any unusual behaviour, or indeed any anomaly at the temperature of the magnetic phase transition.

To date, the effects of magnetism on the lattice parameters and the high-temperature anisotropy of the thermal expansion in fayalite have never been studied together and there have been no detailed measurements of the lattice parameters within the antiferromagnetic region. Using neutron powder diffraction, we have identified the two antiferromagnetic phase transitions and have determined their effects on the cell parameters of synthetic Fe_2SiO_4. The neutron powder data were collected with the High Resolution Powder Diffractometer (HRPD) at the STFC ISIS spallation neutron source. Measurements were made between 10 K and 1453 K, i.e. close to fayalite's melting point at 1478 K, allowing us to investigate the structural basis for the unusual anisotropy of fayalite's thermal expansion.

Experimental method

Sample synthesis

Polycrystalline Fe_2SiO_4 was prepared from a stoichiometric mixture of metallic Fe, Fe_2O_3 and SiO_2. The sample was synthesised using a new WC-COW solid-state oxygen buffering reaction within a ceramic crucible system (Dobson, 2021) that is effective at maintaining the oxygen fugacity at a level between iron–wüstite and quartz–iron–fayalite during solid-state synthesis of Fe-bearing silicates at 1 atm and 1273–1373 K. The sample was sintered for 6 days at 1323 K in a set of nested alumina crucibles inside a 5 L muffle furnace. In total, three sintering cycles were used, each lasting 2 days, with the fayalite being re-ground and pelleted between cycles. The recovered sample was examined by powder X-ray diffraction at room temperature; it was found to contain a very small amount of quartz as an impurity phase, with the Rietveld-refined X-ray diffraction pattern indicating a composition of 99.8 wt.% Fe_2SiO_4 and 0.2 wt.% SiO_2.

Neutron Powder Diffraction

Time-of-flight neutron powder diffraction patterns were collected with the High Resolution Powder Diffractometer (HRPD) (Ibberson *et al.*, 1992; Ibberson 2009) at the STFC ISIS spallation neutron source, Rutherford Appleton Laboratory, UK. Diffraction data, at all temperatures, were collected in HRPD's standard 100 ms wide time-of-flight window in the range 30–130 ms (*d*-spacings = 0.65–2.6 Å), normalised to the incident spectrum and corrected for detector efficiency by reference to a V:Nb standard, and then exported in a format suitable for analysis with *GSAS/EXPGUI* (Larson and Von Dreele, 2000; Toby, 2001) using the Mantid library of diffraction algorithms (Mantid, 2013; Arnold *et al.*, 2014).

For the low-temperature data collection, between 10 and 340 K, the sample was loaded into an 18 mm × 23 mm aluminium-alloy 'slab can' sample holder with a depth of 5 mm. The Al sample holder is open at the front (beam-facing) and rear, and the sample is then contained by 125 μm thick vanadium foil windows, held in place with steel frames and sealed with indium wire. Exposed steel and aluminium surfaces on the front face of the holder were masked from the incident beam with Gd and Cd foils. The sample holder has holes drilled on either side of the specimen area, one to accept a RhFe resistance thermometer, and the other to take a cartridge heater; this arrangement allows rapid and accurate control of the true sample temperature provided that an appropriate time – ~10 minutes – is allowed for thermal equilibration after each change of temperature (Fortes, 2019). The assembly was then loaded into a closed-cycle refrigerator (CCR) held under a partial pressure of ~50 mbar of He exchange-gas. An initial dataset was collected at 100 K, followed by measurements in 5 K increments on cooling to 10 K. Thereafter, the sample was warmed to 110 K and measurements were obtained in 10 K steps up to 340 K. The majority of the datasets were 'short' acquisitions of ~10 minutes duration (8 μAh of proton beam current) intended solely for the refinement of unit-cell parameters, but several longer measurements for ~100 minutes (80 μAh) were made at 40 K and 10 K on cooling and at 300 K on warming;

https://doi.org/10.1180/mgm.2023.66 Published online by Cambridge University Press

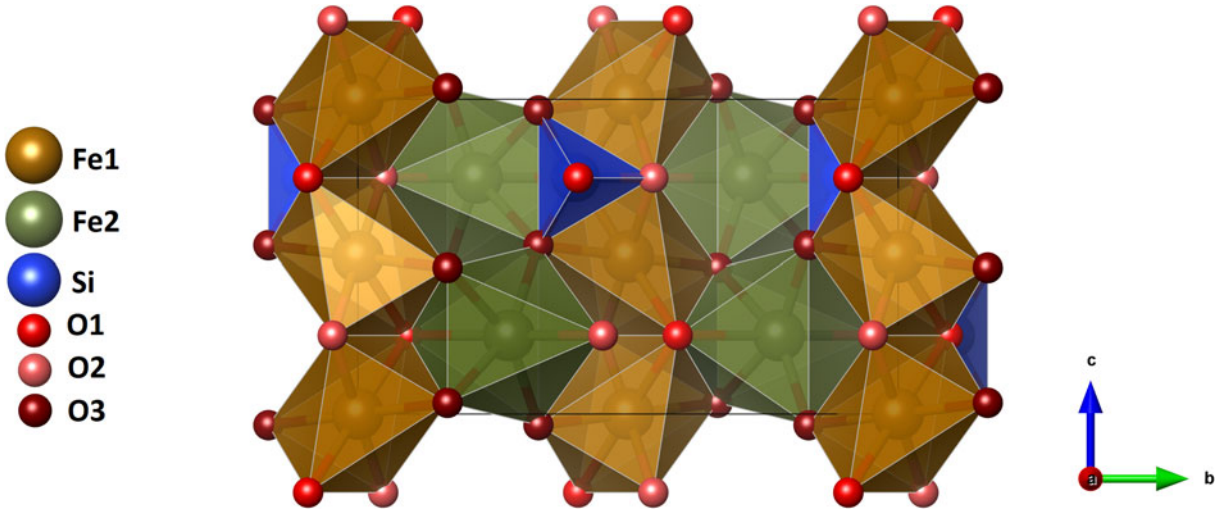

Figure 1. Polyhedral model of the Fe_2SiO_4 structure, consisting of SiO_4 tetrahedra (blue) and Fe1 (= M1, orange) and Fe2 (= M2, green) octahedra, viewed along [100]. Image produced using *VESTA* (Momma and Izumi, 2011).

these provided diffraction data of excellent statistical quality suitable for us to carry out high-precision structure refinements.

To prevent sample degradation in the evacuated furnace at high temperatures, the sample was loaded under He gas at room temperature into a Ti–Zr–Mo alloy ('TZM') cylindrical sample can (8 mm in internal diameter with a 0.25 mm wall thickness), which was then sealed with a niobium wire gasket. This was then placed in a vacuum furnace (10^{-6} mbar) and heated using vanadium-foil elements. Two K-type thermocouples were secured on either side of the sample can. After the first data collection at room temperature, ~297 K (20 μAh), a measurement was made at 373 K (40 μAh), after which data were taken in 20 K increments from 373 K to 1273 K, counting for 10 μAh at each point. As before, longer counting-times were used at 573 K (80 μAh), 873 K (80 μAh) and 1173 K (120 μAh) to provide data more suitable for high-precision structure refinements. The experiment was interrupted by a failure of the furnace elements at ~1270 K, as a result of which the sample cooled rapidly back to room temperature. After the elements were replaced, the sample was reheated, with data collected at 1073 K and 1173 K (to provide an overlap with the first high-temperature dataset), whereafter diffraction patterns were obtained in 20 K intervals from 1273 K up to 1453 K, close to the melting point of Fe_2SiO_4 which is reported to be at 1478 K. In the second high-temperature series, data were collected for 10 μAh at each temperature, except at 1353 K and 1453 K where the counting times were extended to 200 μAh and 167 μAh respectively. After heating to 1453 K, the recovered Fe_2SiO_4 sample, measured at 573 K for 53 μAh, was found to be unaltered, with no additional peaks seen in the powder pattern (the unit-cell parameters of the recovered sample are given in the footnote to Table 2; the refined values of the fractional coordinates differed by 0.0007, at most, from those originally found at 573 K).

Refinement

Neutron diffraction patterns of Fe_2SiO_4 collected at 10 K, 300 K and 1453 K are presented in Fig. 2. A total of 119 data sets were collected for Fe_2SiO_4: 45 in the low- and 75 in the high-temperature sample environment. The good statistical quality of even the 'short' data acquisitions allowed us to carry out refinements of the nuclear and magnetic structure using all of the data collected between 10 and 1453 K. For consistency, the same set of parameters was refined for both the 'long' and 'short' counting times. As one might expect, for the short counting times, the estimated standard deviations of the refined parameters are larger than those derived from the longer measurements, however we are nonetheless able to discern trends in – for example – bond lengths, bond angles and magnetic moments with a high degree of certainty, as illustrated below. The magnetic and nuclear structures were refined as separate phases with the Rietveld method using the *GSAS I* suite of programmes (Larson and Von Dreele, 2000) with the *EXPGUI* graphical interface (Toby, 2001). Consideration of previous studies of the magnetic structure of Fe_2SiO_4 (e.g. Müller *et al.*, 1982) indicated that the space group remains *Pbnm* in all phases and so the magnetic and nuclear unit cells were constrained to be the same throughout. Following Müller *et al.* (1982), for the canted antiferromagnetic (AFM2) region ($T < 23$ K), all three components of the magnetic moment on the Fe1 site were allowed to vary while for the collinear (AFM1) region, $25 \leq T \leq 65$ K, these moments were constrained to remain parallel to the *c* axis; the moments on the Fe2 site were constrained to remain parallel to the *c* axis at all temperatures below 65 K. At and below 65 K, in the AFM1 phase, 59 variables were included in the refinement (one scale factor, six profile parameters, eight background coefficients, three cell parameters, two magnetic moments, 11 fractional coordinates, 28 displacement parameters); below the second AFM transition at 23 K, the number of refined magnetic moments increases to four. For all data collected with the sample in the CCR, the instrumental parameters DIFC and DIFA, which define the primary neutron flight path and the contribution to the path from wavelength-dependent absorption from the sample, were fixed at 48216.25 and −0.38, respectively, these being derived from an instrument calibration carried out using a NIST silicon standard, SRM640e. Above 65 K we observed no peaks from the magnetic cell and therefore only the nuclear phase was refined, including 57 variables. Bragg reflections from the TZM sample can were present in the data collected with the sample in the furnace. This TZM alloy has a composition of ~99.4%

https://doi.org/10.1180/mgm.2023.66 Published online by Cambridge University Press

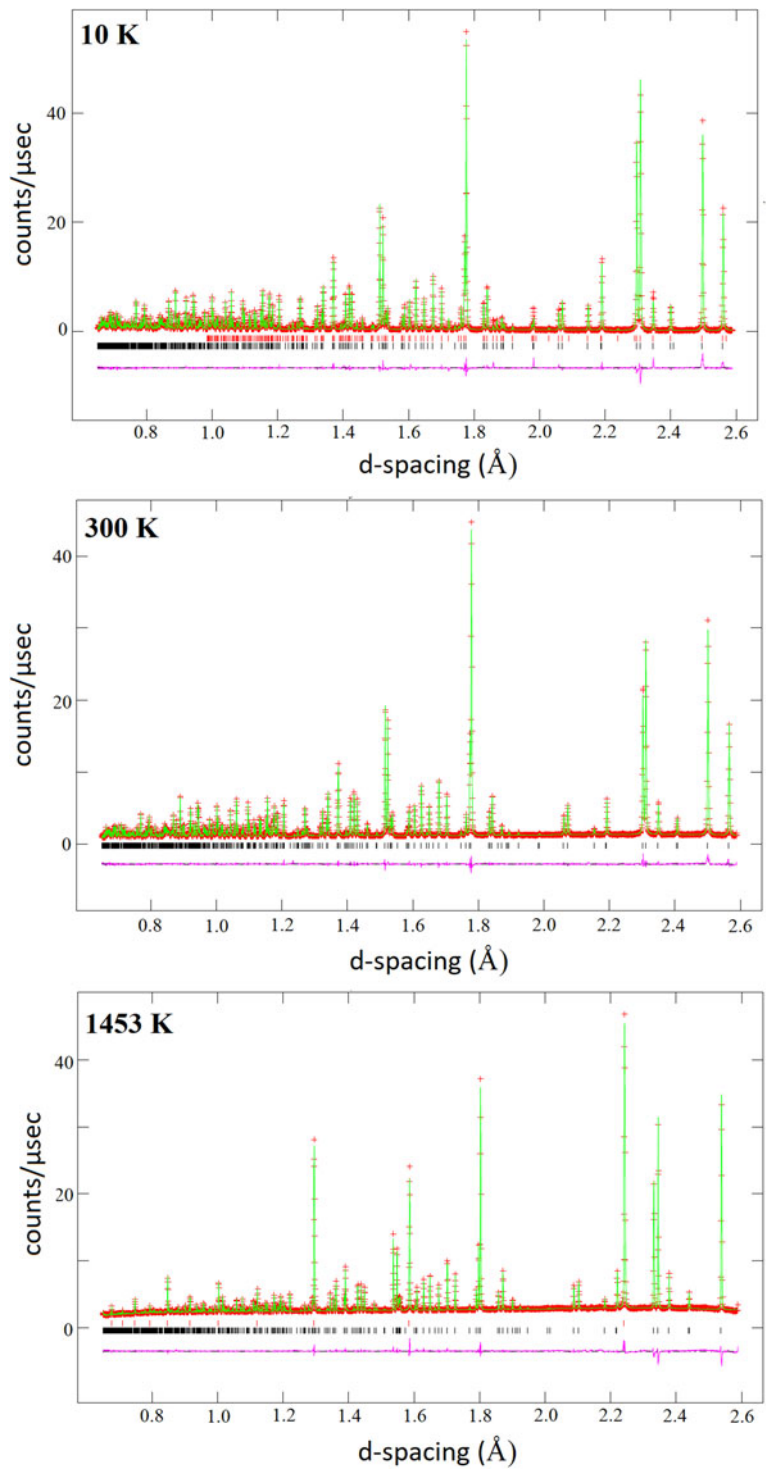

Figure 2. Examples of neutron powder diffraction patterns of Fe_2SiO_4 collected at different temperatures. Observed data are shown as red crosses, the calculated diffraction pattern as a green line, and their differences are given by the lower pink trace. The black tick marks in each of the plots show the positions of the Bragg reflections from the nuclear Fe_2SiO_4 crystal structure. For the refinement at 10 K, the red tick marks show the positions of the Bragg reflections from the Fe_2SiO_4 magnetic structure; the contribution from magnetic scattering to the diffraction pattern is judged negligible below 0.986 Å. For the 1453 K refinement, the red tick marks show the positions of the Bragg reflections from the TZM sample can.

Mo, alloyed with 0.5% Ti, 0.08% Zr and 0.02% C; it was, therefore, included in the refinement on the basis that it had the body-centred cubic structure of Mo, with the intensities calculated via the Le Bail method as it was highly textured. The lattice parameters of Fe_2SiO_4 and those of the Mo sample can, the fractional coordinates, atomic displacement parameters, scale factors, phase fractions, background and profile parameters were refined with DIFC and DIFA (adjusted to take account of the different sample geometry), fixed at 48216.25 and −0.52, respectively. Due to a small offset between the two stages, as well as between the two sets of high-temperature measurements, all high-temperature cell parameter values were scaled to match the low-temperature results. This was done by fitting first-order polynomials to the data from 300–340 K (CCR) and 297–433 K (furnace) and 960–1000 K (first high-temperature run) and 900–1020 K (second high-temperature run) and then calculating the scale factors for the offsets (see Table 2) from the ratios of the values of the polynomials at 300 K and 980 K. Refined fractional coordinates, anisotropic atomic displacement parameters (and their isotropic equivalents) and magnetic moments of the ten data sets with

https://doi.org/10.1180/mgm.2023.66 Published online by Cambridge University Press

Table 1. Fractional coordinates, anisotropic atomic displacements, and magnetic moments at 10 temperature points (numbers in parenthesis are one standard error of the least significant digits).

Closed-Cycle Refrigerator

Temperature 10 K

Atom	*x*	*y*	*z*	$100U^{11}$ (Å^2)	$100U^{22}$ (Å^2)	$100U^{33}$ (Å^2)	$100U^{12}$ (Å^2)	$100U^{13}$ (Å^2)	$100U^{23}$ (Å^2)	U_{iso} (Å^2)*
Fe1	0	0	0	0.29(2)	0.37(2)	0.36(2)	0.02(2)	−0.07(2)	−0.04(1)	0.0034
Fe2	0.98619(4)	0.28012(4)	¼	0.30(2)	0.29(2)	0.31(2)	0.01(2)	0	0	0.0030
Si	0.4313(2)	0.0972(1)	¼	0.36(6)	0.43(5)	0.36(5)	0.08(4)	0	0	0.0038
O1	0.7684(2)	0.0919(1)	¼	0.44(4)	0.57(4)	0.49(3)	0.01(3)	0	0	0.0046
O2	0.2089(2)	0.4528(1)	¼	0.30(4)	0.42(4)	0.55(3)	−0.09(3)	0	0	0.0042
O3	0.2882(1)	0.1658(1)	0.4643(1)	0.46(3)	0.60(3)	0.46(3)	−0.06(2)	0.07(2)	−0.06(2)	0.0051

Site	Mx (μ_B)	My (μ_B)	Mz (μ_B)	|M| (μ_B)
M1	2.46(4)	1.37(7)	3.39(3)	4.41(5)
M2	0	0	4.53(3)	4.53(3)
Chi^2	2.235			
wRp	0.041			

Temperature 40 K

Atom	*x*	*y*	*z*	$100U^{11}$ (Å^2)	$100U^{22}$ (Å^2)	$100U^{33}$ (Å^2)	$100U^{12}$ (Å^2)	$100U^{13}$ (Å^2)	$100U^{23}$ (Å^2)	U_{iso} (Å^2)*
Fe1	0	0	0	0.22(3)	0.33(4)	0.40(3)	0.08(3)	−0.06(3)	−0.08(3)	0.0031
Fe2	0.9859(1)	0.2798(1)	¼	0.25(4)	0.29(4)	0.30(3)	0.04(3)	0.00	0.00	0.0027
Si	0.4307 (3)	0.0972(2)	¼	0.59(10)	0.30(8)	0.36(7)	0.03(6)	0.00	0.00	0.0041
O1	0.7687(3)	0.0920(1)	¼	0.18(7)	0.56(6)	0.57(5)	0.01(5)	0.00	0.00	0.0043
O2	0.2088(3)	0.4529(1)	¼	0.35(6)	0.37(6)	0.44(5)	−0.08(5)	0.00	0.00	0.0038
O3	0.2889(2)	0.1658(1)	0.4642(2)	0.43(4)	0.53(4)	0.43(4)	−0.02(4)	0.07(3)	−0.08(4)	0.0046

Site	Mx (μ_B)	My (μ_B)	Mz (μ_B)	|M| (μ_B)
M1	0	0	2.38(5)	2.38(5)
M2	0	0	4.28(4)	4.28(4)
Chi^2	6.015			
wRp	0.045			

Temperature 100 K

Atom	*x*	*y*	*z*	$100U^{11}$ (Å^2)	$100U^{22}$ (Å^2)	$100U^{33}$ (Å^2)	$100U^{12}$ (Å^2)	$100U^{13}$ (Å^2)	$100U^{23}$ (Å^2)	U_{iso} (Å^2)*
Fe1	0	0	0	0.51(2)	0.69(3)	0.63(2)	0.01(3)	−0.03(2)	−0.11(2)	0.0038
Fe2	0.9861(2)	0.2800(1)	¼	0.55(3)	0.53(3)	0.56(2)	0.03(2)	0.00	0.00	0.0032
Si	0.4315(2)	0.0971(1)	¼	0.74(7)	0.60(6)	0.63(6)	0.12(5)	0.00	0.00	0.0042
O1	0.7680(2)	0.0919(1)	¼	0.52(5)	0.82(4)	0.80(4)	−0.07(4)	0.00	0.00	0.0047
O2	0.2089(2)	0.4529(1)	¼	0.58(5)	0.57(4)	0.82(4)	−0.17(4)	0.00	0.00	0.0043
O3	0.2884(1)	0.1657(1)	0.4643(1)	0.72(3)	0.83(3)	0.66(3)	−0.06(3)	0.08(3)	−0.11(3)	0.0051
Chi^2	3.209									
wRp	0.033									

Temperature 300 K

Atom	*x*	*y*	*z*	$100U^{11}$ (Å^2)	$100U^{22}$ (Å^2)	$100U^{33}$ (Å^2)	$100U^{12}$ (Å^2)	$100U^{13}$ (Å^2)	$100U^{23}$ (Å^2)	U_{iso} (Å^2)*
Fe1	0	0	0	0.92(3)	1.33(4)	1.11(3)	−0.06(4)	−0.16(3)	−0.28(3)	0.0112
Fe2	0.9869(2)	0.2798(1)	¼	1.06(4)	1.03(4)	1.04(3)	0.01(3)	0.00	0.00	0.0104
Si	0.4315(3)	0.0970(2)	¼	1.52(10)	0.78(8)	1.01(7)	0.18(6)	0.00	0.00	0.0110
O1	0.7675(2)	0.0922(1)	¼	0.89(7)	1.41(5)	1.25(6)	−0.03(5)	0.00	0.00	0.0118
O2	0.2101(3)	0.4533(1)	¼	1.14(6)	0.88(5)	1.30(5)	−0.04(5)	0.00	0.00	0.0110
O3	0.2881(2)	0.1657(1)	0.4644(1)	1.12(4)	1.39(4)	1.28(4)	−0.12(4)	0.21(3)	−0.11(4)	0.0126
Chi^2	4.307									
wRp	0.038									

TZM Furnace

Temperature 373 K

Atom	*x*	*y*	*z*	$100U^{11}$ (Å^2)	$100U^{22}$ (Å^2)	$100U^{33}$ (Å^2)	$100U^{12}$ (Å^2)	$100U^{13}$ (Å^2)	$100U^{23}$ (Å^2)	U_{iso} (Å^2)*
Fe1	0	0	0	0.72(5)	1.06(6)	0.89(5)	0.18(6)	−0.07(5)	−0.23(4)	0.0089
Fe2	0.9854(3)	0.2808(1)	¼	0.85(6)	0.70(6)	0.79(5)	0.09(4)	0.00	0.00	0.0078
Si	0.4306(4)	0.0975(2)	¼	0.83(3)	0.76(2)	0.46(10)	0.11(9)	0.00	0.00	0.0068
O1	0.7694(3)	0.0926(2)	¼	0.13(9)	1.18(8)	1.07(9)	−0.21(8)	0.00	0.00	0.0079
O2	0.2090(4)	0.4531(2)	¼	0.57(9)	0.80(9)	1.35(9)	0.11(8)	0.00	0.00	0.0090
O3	0.2891(3)	0.1659(1)	0.4644(2)	0.78(6)	1.37(7)	0.88(6)	0.02(5)	0.22(5)	−0.52(5)	0.0100
Chi^2	2.512									
wRp	0.034									

(*Continued*)

https://doi.org/10.1180/mgm.2023.66 Published online by Cambridge University Press

Table 1. (*Continued.*)

TZM Furnace

Temperature 573 K										
Atom	*x*	*y*	*z*	$100U^{11}$ (Å^2)	$100U^{22}$ (Å^2)	$100U^{33}$ (Å^2)	$100U^{12}$ (Å^2)	$100U^{13}$ (Å^2)	$100U^{23}$ (Å^2)	U_{iso} (Å^2)*
Fe1	0	0	0	0.97(4)	1.62(5)	1.22(5)	0.15(5)	−0.12(5)	−0.27(4)	0.0105
Fe2	0.9867(3)	0.2804(1)	¼	1.30(5)	0.93(5)	1.09(5)	0.16(4)	0.00	0.00	0.0092
Si	0.4305(4)	0.0977(2)	¼	0.51(2)	0.85(10)	0.90(9)	0.05(7)	0.00	0.00	0.0063
O1	0.7679(3)	0.0933(2)	¼	0.38(9)	1.54(8)	1.40(8)	−0.09(7)	0.00	0.00	0.0112
O2	0.2096(3)	0.4534(2)	¼	0.96(8)	1.08(8)	1.74(8)	0.04(7)	0.00	0.00	0.0110
O3	0.2895(2)	0.1655(1)	0.4630(2)	1.06(5)	1.69(6)	1.30(6)	0.05(5)	0.14(5)	−0.59(5)	0.0113
Chi^2	3.274									
wRp	0.027									

Temperature 873 K										
Atom	*x*	*y*	*z*	$100U^{11}$ (Å^2)	$100U^{22}$ (Å^2)	$100U^{33}$ (Å^2)	$100U^{12}$ (Å^2)	$100U^{13}$ (Å^2)	$100U^{23}$ (Å^2)	U_{iso} (Å^2)*
Fe1	0	0	0	1.57(5)	2.64(7)	1.75(5)	−0.01(6)	−0.24(6)	−0.55(5)	0.0200
Fe2	0.9870(3)	0.2814(1)	¼	1.88(6)	1.59(6)	1.85(5)	0.04(5)	0.00	0.00	0.0174
Si	0.4299(4)	0.0975(2)	¼	0.90(3)	1.36(3)	1.48(10)	0.27(9)	0.00	0.00	0.0115
O1	0.7666(3)	0.0936(2)	¼	0.59(10)	2.33(10)	2.33(9)	−0.28(8)	0.00	0.00	0.0165
O2	0.2096(4)	0.4542(2)	¼	1.28(9)	1.31(9)	2.71(10)	0.12(8)	0.00	0.00	0.0170
O3	0.2903(3)	0.1651(1)	0.4629(2)	1.49(6)	2.82(8)	1.84(7)	0.08(6)	0.11(6)	−0.76(6)	0.0201
Chi^2	3.264									
wRp	0.027									

Temperature 1173 K										
Atom	*x*	*y*	*z*	$100U^{11}$ (Å^2)	$100U^{22}$ (Å^2)	$100U^{33}$ (Å^2)	$100U^{12}$ (Å^2)	$100U^{13}$ (Å^2)	$100U^{23}$ (Å^2)	U_{iso} (Å^2)*
Fe1	0	0	0	2.08(6)	3.94(9)	2.61(7)	−0.02(8)	−0.34(7)	−0.96(6)	0.0287
Fe2	0.9877(4)	0.2817(1)	¼	2.89(7)	2.07(7)	2.45(7)	0.01(6)	0.00	0.00	0.0247
Si	0.4307(5)	0.0977(2)	¼	1.44(6)	1.60(5)	1.79(3)	0.10(1)	0.00	0.00	0.0160
O1	0.7650(4)	0.0944(2)	¼	1.01(2)	3.30(2)	2.86(2)	−0.10(10)	0.00	0.00	0.0238
O2	0.2108(4)	0.4546(2)	¼	2.00(2)	1.84(2)	3.47(2)	0.23(9)	0.00	0.00	0.0243
O3	0.2916(3)	0.1652(2)	0.4609(2)	2.17(8)	3.78(10)	2.52(9)	−0.02(7)	0.16(7)	−1.10(7)	0.0282
Chi^2	1.145									
wRp	0.043									

Temperature 1353 K										
Atom	*x*	*y*	*z*	$100U^{11}$ (Å^2)	$100U^{22}$ (Å^2)	$100U^{33}$ (Å^2)	$100U^{12}$ (Å^2)	$100U^{13}$ (Å^2)	$100U^{23}$ (Å^2)	U_{iso} (Å^2)*
Fe1	0	0	0	2.29(1)	4.49(6)	2.67(2)	−0.14(4)	−0.78(9)	−1.04(10)	0.0323
Fe2	0.9874(6)	0.2826(2)	¼	2.77(2)	2.19(2)	2.72(2)	0.16(10)	0.00	0.00	0.0265
Si	0.4318(8)	0.0978(4)	¼	1.14(7)	2.12(6)	1.84(2)	-0.33(8)	0.00	0.00	0.0161
O1	0.7633(6)	0.0938(3)	¼	1.00(1)	3.36(8)	0.21(10)	2.98(7)	0.21(8)	−0.15(7)	0.0256
O2	0.2103(7)	0.4553(3)	¼	1.42(7)	1.82(20)	3.81(?)	0.21(?)	0.37(5)	0.00	0.0261
O3	0.2924(6)	0.1649(3)	0.4607(4)	2.63(2)	3.97(8)	2.50(5)	0.47(3)	0.11(1)	−1.24(2)	0.0305
Chi^2	1.152									
wRp	0.043									

Temperature 1453 K										
Atom	*x*	*y*	*z*	$100U^{11}$ (Å^2)	$100U^{22}$ (Å^2)	$100U^{33}$ (Å^2)	$100U^{12}$ (Å^2)	$100U^{13}$ (Å^2)	$100U^{23}$ (Å^2)	U_{iso} (Å^2)*
Fe1	0	0	0	2.53(6)	4.31(10)	2.34(5)	0.07(9)	−0.62(7)	−1.13(6)	0.0305
Fe2	0.9876(4)	0.2828(1)	¼	3.28(8)	2.30(8)	3.48(6)	0.07(7)	0.00	0.00	0.0301
Si	0.4321(4)	0.0976(3)	¼	0.09(5)	2.13(6)	3.08(5)	−0.08(1)	0.00	0.00	0.0176
O1	0.7654(4)	0.0945(2)	¼	0.56(2)	3.53(3)	3.44(3)	−0.38(10)	0.00	0.00	0.0250
O2	0.2107(4)	0.4562(2)	¼	2.16(3)	1.56(2)	4.31(4)	−0.06(10)	0.00	0.00	0.0267
O3	0.2955(3)	0.1654(2)	0.4578(3)	2.47(7)	4.54(2)	2.61(9)	0.72(8)	−0.10(7)	−0.95(6)	0.0320
Chi^2	5.629									
wRp	0.023									

* Equivalent isotropic displacement parameters calculated from the anisotropic values.

longer collection times, from the CCR and the furnace, are shown in Table 1. The use of anisotropic displacement parameters with powder data is sometimes questionable. However, we believe that they can be justified in this case as we have neutron data extending to 0.65 Å and because the resulting equivalent isotropic displacements (Table 1) are such that the values for the same types of atoms are always very similar. In the high-temperature data, when the scattering at short *d*-spacings is reduced in intensity, the values are probably less reliable, with one component of the displacement ellipsoid of a few atoms for some data sets (e.g. U^{11} for Si and O1 at 1453 K) occasionally taking values that are too small, without, however, showing a systematic trend (Supplementary Fig. 1 shows plots of the displacement ellipsoids).

https://doi.org/10.1180/mgm.2023.66 Published online by Cambridge University Press

Table 2. Lattice parameters and unit-cell volumes* measured in this study. The listed values are unscaled and the numbers in parenthesis are one standard error of the least significant digit.

Closed-Cycle Refrigerator					TZM furnace				
T (K)	*a* (Å)	*b* (Å)	*c* (Å)	V (Å^3)	*T* (K)	*a* (Å)	*b* (Å)	*c* (Å)	V (Å^3)
10	4.81638(1)	10.44704(1)	6.08316(1)	306.086(1)	453	4.82534(2)	10.49135(5)	6.09972(3)	308.794(2)
15	4.81638(2)	10.44709(4)	6.08318(2)	306.088(1)	473	4.82614(2)	10.49337(5)	6.10130(3)	308.985(2)
20	4.81640(2)	10.44725(4)	6.08316(2)	306.093(1)	493	4.82702(2)	10.49530(5)	6.10293(3)	309.181(2)
25	4.81644(2)	10.44743(4)	6.08300(2)	306.095(1)	513	4.82775(2)	10.49697(5)	6.10444(3)	309.353(2)
30	4.81648(2)	10.44784(4)	6.08287(2)	306.101(2)	533	4.82859(2)	10.49879(5)	6.10584(3)	309.532(2)
35	4.81649(2)	10.44827(4)	6.08276(2)	306.109(2)	553	4.82971(2)	10.50112(5)	6.10777(3)	309.770(2)
40	4.81654(2)	10.44887(2)	6.08256(1)	306.120(1)	573	4.83058(1)	10.50321(3)	6.10951(2)	309.976(1)
45	4.81655(2)	10.44923(4)	6.08247(2)	306.126(2)	593	4.83151(2)	10.50515(4)	6.11112(3)	310.174(2)
50	4.81659(2)	10.45006(4)	6.08230(2)	306.145(2)	613	4.83250(2)	10.50721(4)	6.11284(3)	310.386(2)
55	4.81660(2)	10.45094(4)	6.08220(2)	306.166(2)	633	4.83347(2)	10.50914(4)	6.11459(3)	310.594(2)
60	4.81663(2)	10.45208(4)	6.08205(2)	306.194(2)	653	4.83450(2)	10.51124(4)	6.11629(3)	310.809(2)
65	4.81666(2)	10.45370(4)	6.08191(3)	306.236(2)	673	4.83547(2)	10.51301(4)	6.11797(3)	311.009(2)
70	4.81670(2)	10.45518(4)	6.08170(2)	306.274(2)	693	4.83651(2)	10.51515(4)	6.11978(3)	311.231(2)
75	4.81673(2)	10.45603(4)	6.08181(2)	306.303(2)	713	4.83755(2)	10.51739(4)	6.12147(3)	311.451(2)
80	4.81676(2)	10.45649(4)	6.08190(2)	306.324(2)	733	4.83864(2)	10.51937(4)	6.12322(3)	311.669(2)
85	4.81675(2)	10.45709(4)	6.08191(2)	306.341(2)	753	4.83970(2)	10.52159(4)	6.12528(3)	311.899(2)
90	4.81680(2)	10.45748(4)	6.08192(3)	306.356(2)	773	4.84070(2)	10.52340(4)	6.12664(3)	312.095(2)
95	4.81685(2)	10.45791(4)	6.08202(3)	306.379(2)	793	4.84170(2)	10.52557(5)	6.12834(3)	312.313(2)
100	4.81686(1)	10.45838(2)	6.08214(1)	306.397(1)	813	4.84206(2)	10.52776(5)	6.13010(3)	312.536(2)
110	4.81702(2)	10.45930(4)	6.08231(3)	306.443(2)	833	4.84389(2)	10.53000(5)	6.13191(3)	312.765(2)
120	4.81708(2)	10.46027(4)	6.08255(3)	306.487(2)	853	4.84495(2)	10.53224(6)	6.13354(4)	312.983(2)
130	4.81720(2)	10.46125(4)	6.08284(2)	306.538(2)	873	4.84600(1)	10.53433(3)	6.13530(2)	313.211(1)
140	4.81736(2)	10.46217(4)	6.08315(2)	306.591(2)	893	4.84710(2)	10.53654(5)	6.13704(3)	313.432(2)
150	4.81747(2)	10.46313(4)	6.08346(3)	306.642(2)	913	4.84820(2)	10.53888(4)	6.13884(3)	313.663(2)
160	4.81770(2)	10.46415(4)	6.08378(3)	306.702(2)	933	4.84934(2)	10.54111(4)	6.14054(3)	313.889(2)
170	4.81791(2)	10.46512(4)	6.08417(3)	306.763(2)	953	4.85044(2)	10.54355(5)	6.14231(3)	314.123(2)
180	4.81804(2)	10.46618(4)	6.08456(3)	306.823(2)	973	4.85156(2)	10.54594(5)	6.14407(3)	314.357(2)
190	4.81830(2)	10.46728(4)	6.08493(3)	306.890(2)	993	4.85272(2)	10.54851(5)	6.14579(3)	314.597(2)
200	4.81851(2)	10.46824(4)	6.08540(3)	306.955(2)	1013	4.85382(2)	10.55107(5)	6.14765(3)	314.840(2)
210	4.81876(2)	10.46938(4)	6.08590(3)	307.030(2)	1033	4.85490(2)	10.55355(5)	6.14945(3)	315.079(2)
220	4.81896(2)	10.47044(4)	6.08637(3)	307.098(2)	1053	4.85608(2)	10.55598(5)	6.15124(3)	315.317(2)
230	4.81916(2)	10.47145(4)	6.08691(3)	307.168(2)	1073	4.85723(2)	10.55847(5)	6.15300(3)	315.556(2)
240	4.81946(2)	10.47250(4)	6.08746(3)	307.245(2)	1093	4.85833(2)	10.56107(5)	6.15470(3)	315.793(2)
250	4.81969(2)	10.47360(4)	6.08791(3)	307.315(2)	1113	4.85944(2)	10.56359(5)	6.15649(3)	316.032(2)
260	4.81996(2)	10.47469(4)	6.08856(3)	307.397(2)	1133	4.86056(2)	10.56612(5)	6.15830(3)	316.273(2)
270	4.82028(2)	10.47566(4)	6.08910(3)	307.473(2)	1153	4.86174(2)	10.56885(5)	6.16009(3)	316.524(2)
280	4.82056(2)	10.47683(4)	6.08967(3)	307.554(2)	1173	4.86288(2)	10.57153(3)	6.16194(2)	316.773(1)
290	4.82087(2)	10.47776(4)	6.09036(3)	307.636(2)	1193	4.86401(2)	10.57424(5)	6.16372(3)	317.020(2)
300	4.82113(1)	10.47890(2)	6.09092(1)	307.714(1)	1233	4.86635(2)	10.57985(5)	6.16750(3)	317.535(2)
310	4.82144(2)	10.47997(4)	6.09154(3)	307.796(2)	1253	4.86761(2)	10.58297(5)	6.16946(3)	317.812(2)
320	4.82175(2)	10.48097(4)	6.09213(3)	307.875(2)	1273	4.86910(2)	10.47885(5)	6.17170(3)	318.131(2)
330	4.82206(2)	10.48199(4)	6.09283(3)	307.961(2)	1293	4.87082(2)	10.48498(5)	6.09264(2)	318.500(2)
340	4.82240(4)	10.48305(9)	6.09356(6)	308.051(4)	1353	4.87444(1)	10.58785(2)	6.16350(1)	319.296(1)
297	4.82023(2)	10.47688(4)	6.08971(3)	307.536(2)	1373	4.87569(2)	10.59065(5)	6.17250(2)	319.569(2)
373	4.82260(2)	10.48435(3)	6.09448(2)	308.148(1)	1393	4.87691(2)	10.59377(5)	6.17425(2)	319.847(2)
393	4.82326(3)	10.48609(5)	6.09572(3)	308.304(2)	1413	4.87810(2)	10.59651(5)	6.17618(2)	320.125(2)
413	4.82397(3)	10.48792(5)	6.09713(3)	308.474(2)	1433	4.87940(2)	10.59957(5)	6.17798(2)	320.401(2)
433	4.82462(2)	10.48967(5)	6.09845(3)	308.635(2)	1453	4.88080(1)	10.60266(3)	6.17988(1)	320.708(1)

*Notes: The values listed in the Table are taken directly from the Rietveld refinements. In subsequent analyses of the cell parameters, the CCR data used were those shown above, with the following multiplicative scale factors then applied to correct for the small offsets between the different sample environments: (1) between the CCR and the high-temperature furnace for *a*, *b*, *c* axes and unit-cell volume, respectively: 1.000199, 1.000139, 1.000198 and 1.000536; (2) between the two high-temperature measurements for *a*, *b*, *c* axes and unit-cell volume, respectively: 0.99984, 0.999856, 0.99982 and 0.999526.

The cell parameters of the 'recovered' sample (i.e. after it had been heated to 1453 K) at 573 K were found to be $a = 4.83072(2)$ Å, $b = 10.50281(4)$ Å, $c = 6.11305(2)$ Å and $V = 310.152(1)$ Å^3; the small differences between these values and those shown at 573 K in the Table are readily attributable to the change in sample environment.

The crystallographic information files have been deposited with the Principal Editor of *Mineralogical Magazine* and are available as Supplementary material (see below).

Results and Discussion

Antiferromagnetic Transition Temperatures

Although the space group of the paramagnetic, canted, and collinear AFM phases of Fe_2SiO_4 remains *Pbnm*, some reflections that are systematically absent when only the nuclear scattering is considered become visible in the collinear AFM and canted AFM phases. To determine the temperature of the transition between the paramagnetic and AFM1 phases, we considered the behaviour of the 052 reflection, as this peak, with intensity coming solely from the magnetic scattering, occurs at a *d*-spacing (~1.72 Å) where it is well separated from other peaks in the diffraction pattern (Fig. 3). The values of $|F_{obs}|^2$ for 052, obtained from the *GSAS* refinements, are shown as a function of temperature in Fig. 3, with those for $T \geq 50$ K fitted by non-linear least squares to the

https://doi.org/10.1180/mgm.2023.66 Published online by Cambridge University Press

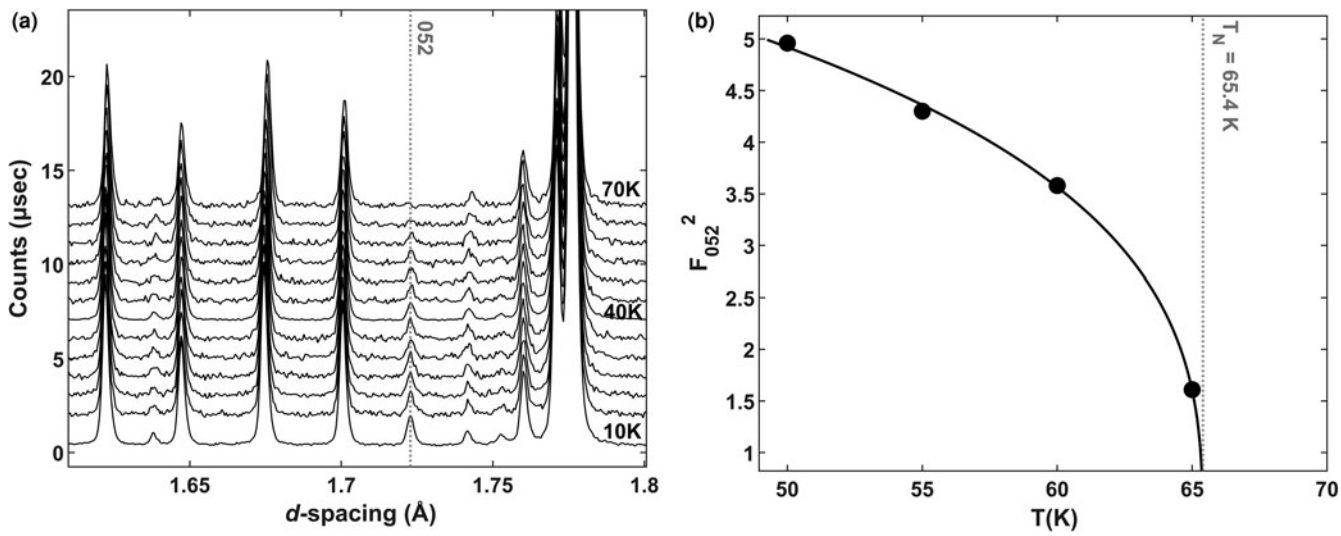

Figure 3. (a) Stacked diffraction patterns from 10 K (bottom-most) to 70 K (top-most) showing the magnetic reflection at 1.72 Å (hkl = 052) and (b) $|F_{obs}|^2$ for the 052 reflection as a function of temperature fitted to equation 1 (solid black line) giving a transition temperature T_N = 65.4(1) K.

expression:

$$|F_{obs}|^2 = A\left(\frac{T - T_N}{T_N}\right)^{\beta} \quad (1)$$

where A is a scale factor, T_N is the transition temperature and β is a critical exponent. Although our data are rather sparse, it can be seen that an excellent fit is obtained, with T_N = 65.4(1) K and β = 0.31(3). Our calculated T_N is in good agreement with previous measurements, which lie in the range 64.9–65.3 K (e.g. Lottermoser *et al.*, 1986; Müller *et al.*, 1982; Suzuki *et al.*, 1981; Santoro *et al.*, 1966; Aronson *et al.*, 2007). Determination of the transition temperature between the AFM1 and AFM2 antiferromagnetic phases from our diffraction patterns is more problematic as no additional, non-overlapped, reflections appear in the AFM2 phase. Thus, although this transition is visible in the behaviour of the *a* and *c* axes, and in the refined values of the magnetic moments on the Fe atoms (see below), we do not consider that we can reliably fix the transition temperature beyond saying that it occurs at $20 \leq T \leq 25$ K; in our analysis of the lattice parameters we have, therefore, adopted the value of 23 K quoted by previous authors (e.g. Müller *et al.*, 1982).

Lattice parameters and thermal expansion

The evolution of the unit-cell volume of Fe_2SiO_4 over the full temperature range is plotted in Fig. 4 and listed in Table 2. Our results are in good agreement with those of earlier high-temperature X-ray diffraction and dilatometry studies (Suzuki *et al.*, 1981; Kroll *et al.*, 2012; Hazen, 1977). The detailed low-temperature behaviour of the unit-cell lattice parameters and volume have not, until now, been reported.

To describe thermal expansion at high temperatures an equation of the form suggested by Fei (1995) is commonly used. In this formulation, the unit-cell volume is given by:

$$V(T) = V_{T_R} exp\left[\int_{T_R}^{T} a_V(T)dT\right] \quad (2)$$

where V_{T_R} is the volume at a reference temperature (in this case T_R = 297 K) and $a_V(T)$ is the volumetric thermal expansion coefficient given by a polynomial expression of the form

$$a_V(T) = a_0 + a_1 T + a_2 T^{-2} \quad (3)$$

The resulting values for all data between 297 K and 1453 K, fitted in *EoSFit7c* (Angel *et al.*, 2014), are V_{T_R} = 307.73(1) Å^3, $a_0 = 3.02(6)\times10^{-5}$ K^{-1}, $a_1 = 0.86(5)\times10^{-8}$ K^{-2}, and $a_2 = -0.97(8)$ K.

A more physically meaningful interpretation of the temperature dependence of the unit-cell volume, encompassing its full temperature range, can be obtained by using Grüneisen approximations to the zero-pressure equation of state (Wallace, 1998). This approach, in which the effects of the thermal expansion are considered to be equivalent to the elastic strain induced by the thermal pressure, also allows estimates of the Debye temperature and Grüneisen parameters. Specifically, the second-order approximation, is more appropriate for covering a wide temperature range (e.g. Vočadlo *et al.*, 2002; Wood *et al.*, 2002; Lindsay-Scott *et al.*, 2007; Hunt *et al.*, 2017) and takes the form:

$$V(T) = \frac{V_0 U}{Q - bU} + V_0 \quad (4)$$

where: $Q = \frac{V_0 K_0}{\gamma}$ and $b = \frac{(K_0' - 1)}{2}$, V_0 is the unit-cell volume at T = 0 K, γ is a Grüneisen parameter which is assumed to be constant and K_0 and K_0' are the bulk modulus and its first derivative with respect to pressure (P) at T = 0 K and P = 0 GPa. The internal energy, $U(T)$, can be calculated using the Debye approximation to describe the energy of thermal vibrations (e.g. Cochran, 1973).

$$U(T) = 9Nk_B T\left(\frac{T}{\theta_D}\right)^{3}\int_0^{3\theta_D/T}\frac{x^3}{\exp(x) - 1}dx \quad (5)$$

Where N is the number of atoms in the unit-cell (in this case N = 28); θ_D is the Debye temperature, and k_B is Boltzmann's constant.

However, in the case of Fe_2SiO_4, the behaviour of the unit-cell volume and lattice parameters is more complex than that which is

https://doi.org/10.1180/mgm.2023.66 Published online by Cambridge University Press

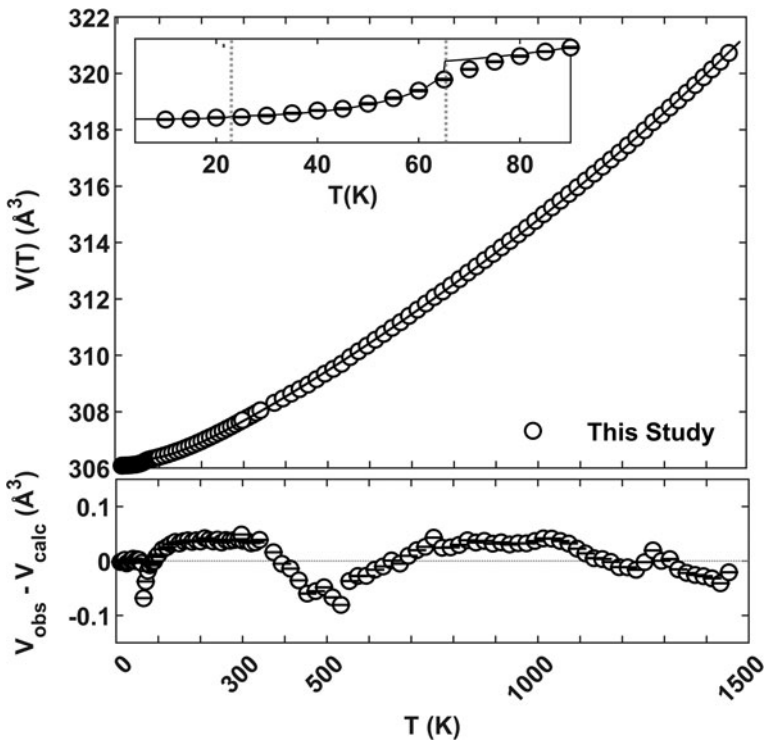

Figure 4. Measured unit-cell volumes of Fe_2SiO_4 against temperature. Experimental data are shown as open circles and the model of equation 6 as a solid black line. Unit-cell volume error bars are omitted because they are smaller than the symbols; the smaller inner panel shows the fit of equation 6 below 90 K in more detail. The lower panel shows the differences between measured and calculated unit-cell volumes as a function of temperature when employing the model of equation 6.

describable by equation 4 because of the magnetostriction resulting from the two magnetic transitions. In previous work on ferromagnetic Fe_3C (Wood *et al.*, 2004) we have accurately modelled $V(T)$ over the full temperature range by assuming that the structural, $V_G(T)$, and magnetic, $V_M(T)$, contributions to the thermal expansion may be separated, i.e., that

$$V(T) = V_G(T) + V_M(T) \tag{6}$$

where $V_G(T)$ was described in a similar way to equation 4. The magnetic contribution, $V_M(T) = 0$ above the temperature at which magnetic ordering occurs; at temperatures below the ferromagnetic phase transition, a mean-field model was used to describe the spontaneous magnetisation, M_S, which was then assumed to induce a change in volume that was proportional to M_S^2. For ferromagnetic systems, such as Fe_3C, symmetry dictates that there can be no coupling between the unit-cell dimensions and any odd power of the spontaneous magnetisation, as otherwise reversal of the magnetisation would reverse the sign of the change in the lattice parameters; thus, the lowest-order coupling is to M_S^2. In a simple antiferromagnet, however, this restriction does not apply as the crystal contains equal numbers of atoms with magnetic moments of opposite sign and thus linear coupling between the cell parameters and the spontaneous magnetisation is allowed, assuming that M_S is here taken to be the moment of one of the sets of oppositely-magnetised atoms.

Fe_2SiO_4 is, though, a more complex material than either Fe_3C or a simple antiferromagnet, in that there are two magnetic transitions with each of the antiferromagnetic phases having two independent sets of magnetic moments. In addition, there is evidence, from e.g. the intensity of the 052 reflection, that the behaviour close to T_N for the paramagnetic to collinear AFM transition is not mean-field like. Nonetheless, we have found that a model based on a modified mean-field magnetisation curve is adequate to allow us to describe the behaviour of the unit-cell volume of Fe_2SiO_4 at low temperature with sufficient accuracy and thereby separate the effects of thermal vibration and of magnetic ordering on the unit-cell volume. We assume that the magnetostrictive contribution to $V(T)$ results from an effective spontaneous magnetisation, M_S, which may be described by the following equation:

$$V_M(T) = A_{65}[M_{S_{65}}(T_{N_{65}})]^{2\beta} + A_{23}[M_{S_{23}}(T_{N_{23}})]^{2\beta} \tag{7}$$

where A_{65} and A_{23} are constants of proportionality, $T_{N_{65}}$ and $T_{N_{23}}$ the transition temperatures and β is an exponent (assumed to be the same for both phase transitions, with the factor of 2 introduced so as to ensure that a value of β = ½ would correspond to mean-field behaviour). To obtain $M_S(T)$ in a mean-field approximation (e.g. Blundell, 2001) it is necessary to solve the following equation:

$$m = B_{\frac{1}{2}}\left(\frac{m}{t}\right) = \tanh\left(\frac{m}{t}\right)$$

where m is the reduced spontaneous magnetisation (i.e. $M_S(T)/M_S(0\ K)$) and $t = T/T_N$. The right side of this equation is the Brillouin function $B_J(y)$ calculated here for $J = ½$, as this is known to provide a good fit to the magnetisation curves of materials containing Fe and other ferromagnetic transition elements (e.g. Dekker, 1964). The theoretical justification for this approach to quantifying the spontaneous magnetostriction is, perhaps, somewhat scant, but equation 7 does result in a curve with the correct asymptotic behaviour as T approaches 0 K and which is also capable of describing the behaviour at temperatures close to T_N. The black solid line in Fig. 4 shows the result obtained from fitting the data to equation 6 by a weighted non-linear least-squares algorithm. The resulting values of the six fitted parameters were: $V_0 = 306.280(9)$ Å^3, $\theta_D = 498(9)$ K, $Q = 4.0(1) \times 10^{-17}$ J, $b = 5.90(1)$, $A_{65} = -0.183(1)$ Å^3, $A_{23} = -0.009(3)$ Å^3

https://doi.org/10.1180/mgm.2023.66 Published online by Cambridge University Press

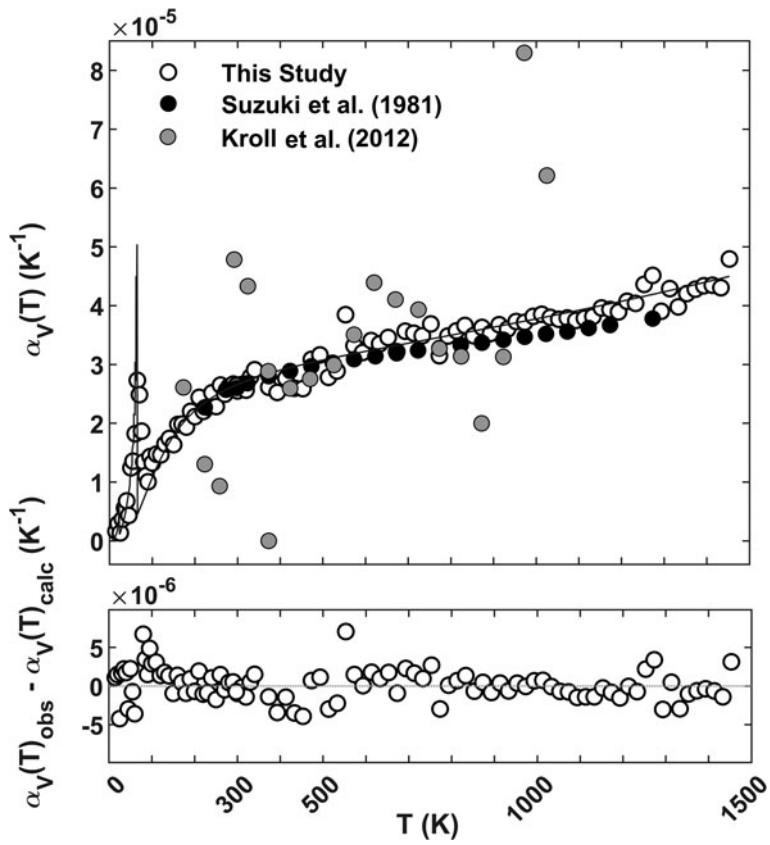

Figure 5. Volumetric thermal expansion coefficient of Fe_2SiO_4 as a function of temperature. Open circles were obtained by point-by-point numerical differentiation of the experimental unit-cell volume data reported in Table 2 and Fig. 3. The solid black line represents the fitted model as calculated by differentiation of equation 6. Grey and black symbols refer to experimental data from previous studies (grey, Kroll *et al.*, 2012; black, Suzuki *et al.*, 1981).

and $\beta = 0.315(3)$. It can be seen that the model of equation 6 provides a good description of the behaviour of the unit-cell volume over the full temperature range of the experiment and that the effect of the 23 K transition on the unit-cell volume is very small. The quality of the fit is also reflected in the volumetric thermal expansion curve, Fig. 5, calculated from

$$a_V(T) = \frac{1}{V(T)}\left(\frac{\partial V}{\partial T}\right)_P \tag{8}$$

The full line in Fig. 5 is obtained by differentiation of equation 6 whereas the points show the results from simple numerical differentiation by differences, point by point, of the $V(T)$ data. Once again, the agreement between model and data is good, despite the deficiencies of the theory. In particular, the neglect of anharmonicity can lead to an underestimate of the thermal expansion coefficient at high temperatures (e.g. Wood *et al.*, 2002), but there is little indication of this in the present case.

For $T > \theta_D$, our volume thermal expansion has slightly higher values compared to those in the literature, with the value of $\alpha_V(T)$ of Suzuki *et al.* (1981) at 1000 K being 9.3% smaller than ours, while those of Kroll *et al.* (2012), when calculated on a point-by-point basis, are scattered. Kroll *et al.* (2012) measured the thermal expansion by single-crystal X-ray diffraction and Suzuki *et al.* (1981) used dilatometry. We consider our data to be more accurate than those of Kroll *et al.* (2012) as we have the advantages of neutron diffraction data collected at a very high Bragg angle on a time-of-flight diffractometer with an extremely long flight path. The time-of-flight method gives us a resolution in *d*-spacing which is effectively constant across the whole of the diffraction pattern, unlike the angle-dispersive X-ray diffraction method used by Kroll *et al.* (2012), in which measurements at very high Bragg angles would be required to obtain comparable resolution. The differences between our results and those of Suzuki *et al.* (1981) may be due to differences in the stoichiometry of the samples, although it should be remembered that dilatometry and diffraction sample fundamentally different properties of the material (see e.g. Simmons and Balluffi, 1962).

The Debye temperature of Fe_2SiO_4 obtained from the fit to equation 6, 498(9) K, is in very good agreement with that reported by Anderson and Suzuki (1983), 510 K, or Anderson and Isaak (1995), 511 K, but somewhat lower than that of Suzuki *et al.* (1981), 565 K. The value of V_0, 306.280(9) Å^3, corresponds to the volume that the unit-cell of a paramagnetic phase of Fe_2SiO_4, with disordered local magnetic moments, would occupy if such a phase persisted to limiting low temperature. An estimate of the incompressibility, K_0, can be obtained directly from the coefficient Q, provided that the Grüneisen parameter is known. Suzuki *et al.* (1981) found γ equal to 1.097(5). If we apply this value of γ we obtain $K_0 = 143(4)$ GPa which is a little larger than published values for K_0, obtained directly from high-pressure studies, which lie between 128 and 136 GPa (e.g. Graham *et al.*, 1988; Béjina *et al.*, 2019, 2021; Speziale *et al.*, 2004; Zhang, 1998; Zhang *et al.*, 2017). The first derivative of the incompressibility with respect to pressure can also be estimated from the coefficient b. The resulting value, $K_0' = 12.8(2)$, is, however, higher than those published from high-pressure studies, which range between 4.1 and 5.3 (e.g. Graham *et al.*, 1988; Béjina *et al.*, 2019, 2021; Speziale *et al.*, 2004; Zhang, 1998). This is an indication of the limitations of the model of equation 6 that are reflected in the fitted parameters. In the $V_G(T)$ term of equation 6 the coefficients Q and b are assumed to be temperature independent, whereas, in reality, the Grüneisen parameter, the

https://doi.org/10.1180/mgm.2023.66 Published online by Cambridge University Press

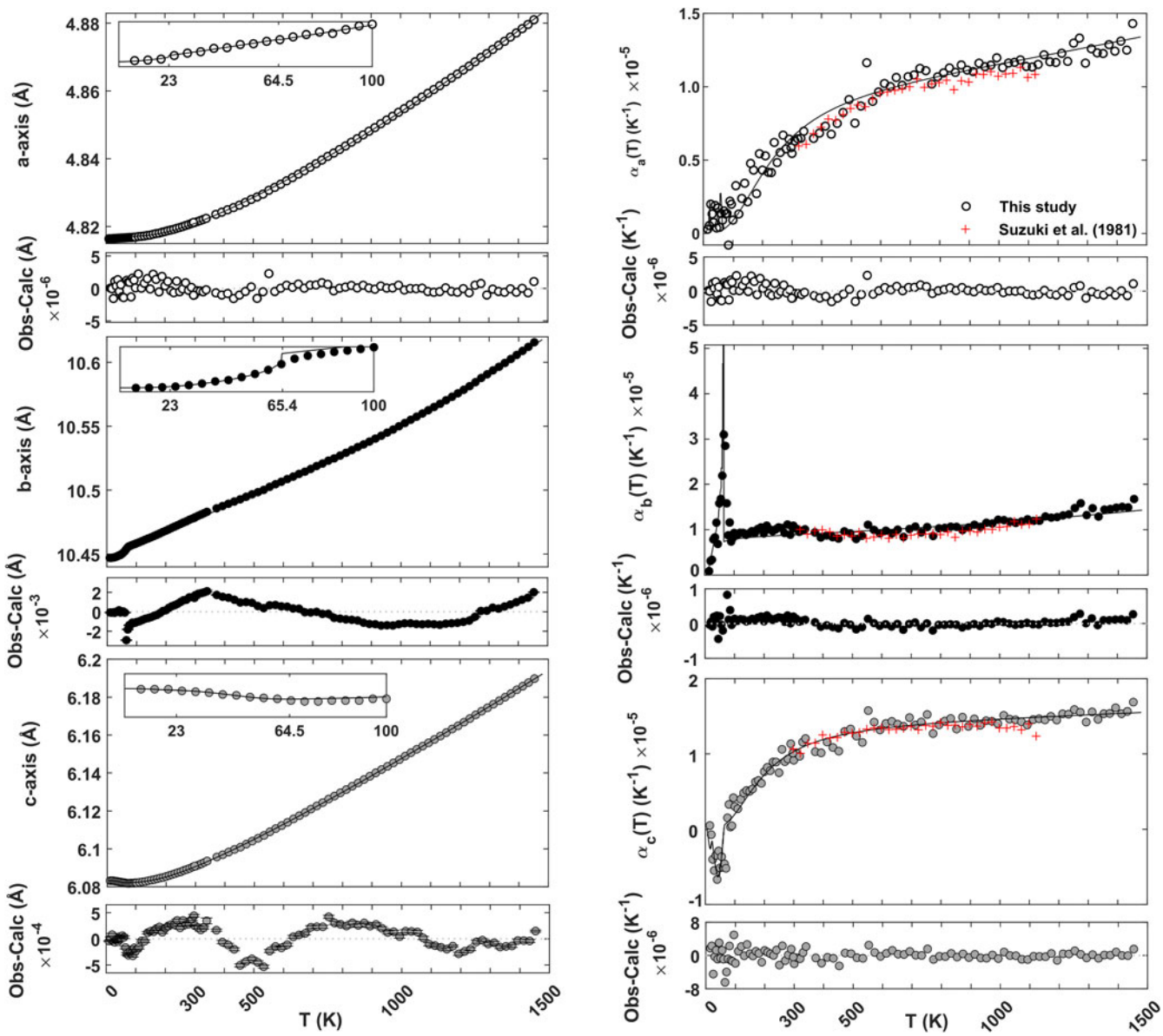

Figure 6. (Left column) Lattice parameters of Fe_2SiO_4 as a function of temperature. Symbols denote the experimental data, as obtained from the Rietveld refinement, and the solid black lines show the fit of the model of equation 9 to the data. Error bars are smaller than the symbols. (Right column) Axial expansivities as a function of temperature (circles), compared to those of Suzuki *et al.* (1981; red crosses). The solid black line represents the fitted model as calculated by differentiation of equation 9; the points were obtained by point-by-point numerical differentiation of the experimental data. The lower panels show the differences between the observed and calculated values.

incompressibility and its first derivative with respect to pressure all have some temperature dependence (e.g. Vočadlo *et al.*, 2002).

A modification of equation 6 can be used to model the anisotropic axial expansivities in Fe_2SiO_4.

$$X(T) = X_G(T) + X_M(T) \tag{9}$$

For the structural term, $X_G(T)$, a modification of the Grüneisen approximation, was used (see Lindsay-Scott *et al.*, 2007).

$$X_G(T) = \frac{X_0 U}{Q_X - b_X U} + X_0 \tag{10}$$

Where $Q_X = K_{X_0} V_0/\gamma$, with the subscript X indicating that we are considering axial rather than volumetric expansion. For an orthorhombic crystal, the expression for the parameter b_X becomes more complex than is for the case of volumetric expansion. Taking as an exemplar the a axis of Fe_2SiO_4 we have $Q_a = K_{a_0} V_0/\gamma$ and $b_a = [K'_{a_0} - 2(K_{a_0}/K_{b_o}) - 2(K_{a_0}/K_{c_o}) - 1]/2$. The axial incompressibilities are related to the elastic compliances, s_{ij}, such that for example, $K_{a_0} = 1/(s_{11} + s_{12} + s_{13})$. Similar equations can be derived for the b and c axes. The magnetic, $X_M(T)$, term of equation 9 takes the same form as was used in equation 6. Therefore equation 9 can be used to fit the data for $a(T)$, $b(T)$ and $c(T)$. The results are plotted in Fig. 6 and Table 3 lists the values of all fitted parameters.

For an orthorhombic crystal, the bulk incompressibility, K_0, and the axial incompressibilities are related by $K_0 = 1/(1/K_{a_0} + 1/K_{b_0} + 1/K_{c_0})$. Assuming that a value of

https://doi.org/10.1180/mgm.2023.66 Published online by Cambridge University Press

Table 3. Fe_2SiO_4 fitted parameters of equation 6 and equation 9 to unit-cell axes and volume data (numbers in parenthesis are one standard error of the least significant digits).

Axis	X_0 (Å)	θ_D (K)	Q (J)	B	A_{65} (Å)	A_{23} (Å)	β
a	4.817(4)	952(3)	$1.14(5)\times10^{-16}$	12.26(6)	−0.000501(3)	−0.000102(2)	0.271(6)
b	10.451(5)	14(1)	$1.45(3)\times10^{-16}$	22.28(1)	−0.0058(60)	0.00080(2)	0.251(3)
c	6.082(5)	791(2)	$8.19(12)\times10^{-17}$	3.52(1)	0.001112(5)	0.00013(8)	2.606(1)
V	306.280(9)	498(9)	$4.0(1)\times10^{-17}$	5.90(1)	−0.183(1)	−0.009(3)	0.315(3)

$\gamma = 1.097$ (Suzuki *et al.*, 1981) applies in all cases, we obtain axial incompressibilities of 408(17), 519(18) and 293(7) GPa for the *a*, *b*, and *c* axes, respectively. By combining the axial incompressibilities we obtain a value of 128(12) GPa for K_0, which is in excellent agreement with values reported in the literature (128–136 GPa – see above), but 6.3% smaller than that obtained by fitting the $V(T)$ data.

Inspection of Fig. 6 reveals that although equation 9 adequately represents the behaviour of the *a* and *c* axes, the same is not true for the *b* axis. The misfits between the model and the observed data for $b(T)$ are much greater than for either $a(T)$ or $c(T)$ and some of the fitted parameters for $b(T)$ are not physically sensible; in particular, the value of the Debye temperature, 14(1) K, is extremely low, reflecting the fact that equation 9 is not able to account satisfactorily for the observed trend. This failure is, perhaps, more clearly seen by examination of the thermal expansion coefficient for the *b* axis, which does not show the expected fall-off below room temperature, instead remaining almost constant until the transition to the AFM1 phase is reached (Fig. 6). The expansion coefficient for the *b* axis that we report here corresponds very closely to that observed above room temperature by Suzuki *et al.* (1981) using single-crystal dilatometry, however our new data reveal that its unusual behaviour continues to much lower temperatures.

A further deficiency of the model defined by equation 9, as applied to the individual cell parameters of fayalite, is revealed by comparison of our derived axial incompressibilities with those measured directly, at room temperature and high pressure, by X-ray diffraction by Zhang (1998) and Zhang *et al.* (2017). Zhang (1998) reported axial incompressibilities of 741, 304 and 568 GPa for the *a*, *b* and *c* axes respectively; Zhang *et al.* (2017) adopted a value of 135 GPa for the volumetric incompressibility and obtained axial values of 682(67), 281(24) and 479(24) GPa. Although our values for the volumetric incompressibility (143(4) K from the fit to $V(T)$ and 128(12) GPa from fitting the axes) agree well with those listed in table 2 of Zhang *et al.* (2017), the agreement for the individual axes is not good, even to the extent of being unable to determine correctly the relative order of incompressibility. Both Zhang (1998) and Zhang *et al.* (2017) have $K_{a_0} > K_{c_0} > K_{b_0}$, whereas from equation 9 we obtain $K_{b_0} > K_{a_0} > K_{c_0}$. Bearing in mind the unusual form of the thermal expansion of the *b* axis, this result is, perhaps, not surprising. As we intend to discuss in a future accompanying paper, in this respect fayalite behaves very differently from forsterite, in which the three crystallographic axes all show the expected reciprocal relationship between thermal expansion coefficient and incompressibility.

Magnetic structures and spontaneous magnetostriction

Our neutron data are consistent with previous results for fayalite (e.g. Santoro *et al.*, 1966; Müller *et al.*, 1982; Lottermoser *et al.*, 1986) showing that below the antiferromagnetic phase transitions at 65.4 K (to the AFM1 structure) and ∼23 K (to AFM2) the magnetic cell remains equal to the crystallographic (chemical) cell and the space group remains *Pbnm*. The magnetic moments of the Fe2 ions are antiferromagnetically coupled and constrained by symmetry (as the Fe2 sites are on mirror planes) to lie parallel/antiparallel to the *c* axis in both the AFM1 and AFM2 structures (Fig. 7). For the Fe1 sites, which lie on centres of symmetry, there is no symmetry constraint on the spin orientation, however the four Fe1 sites in the unit cell are related by symmetry such that there is no net magnetic moment. Previous neutron diffraction studies on powder samples (Santoro *et al.*, 1966) and with single crystals (Müller *et al.*, 1982; Lottermoser *et al.*, 1986) have shown that in the AFM1 phase the moments of the Fe1 and Fe2 sites are collinear, but in the AFM2 phase the moments on the Fe1 sites are canted. Santoro *et al.* (1966; see also Lottermoser *et al.*, 1986) described two possible models for the spin canting on the Fe1 site, only one of which (that originally proposed by Cox *et al.*, 1965) would seem to be consistent with space group *Pbnm*. Given that the symmetry is unchanged on passing from the AFM1 to the AFM2 phase, there has been some discussion, on the basis of results from single-crystal neutron diffraction (Lottermoser *et al.*, 1986; Fuess *et al.*, 1988), as to whether there was a distinct transition between the two phases or whether there was, instead, just a gradual change of the canting angle accompanied by a decrease of the magnetic moments. However, an analysis of Fe_2SiO_4 magnetisation and its anisotropy by Ehrenberg and Fuess (1993), indicated a change in spin canting direction on the Fe1 sites below ∼20 K which is consistent with Mössbauer experiments on temperature-dependent hyperfine fields (e.g. Hafner *et al.*, 1990; Lottermoser *et al.*, 1995, 1996).

Our refinements of the AFM2 magnetic structure were based on the model proposed by Cox *et al.* (1965), and later confirmed by Müller *et al.* (1982) and Lottermoser *et al.* (1986); in our refinements of the AFM1 structure, the moments of the Fe1 ions were constrained to lie along the *c* axis. As discussed by Cococcioni *et al.* (2003 – see their figure 2), there are, however, two possible configurations for the relative orientation of the moments on the Fe1 and Fe2 sites. We found that the arrangement shown in Fig. 7 gave the best fit to our data; this arrangement also corresponds to the ground state of the system, as determined by quantum-mechanical modelling (Cococcioni *et al.*, 2003), with the magnetisation of the Fe2 ion being in the same direction to that of its closest Fe1 ion, an arrangement suggesting antiferromagnetic ordering that occurs between corner-sharing octahedra.

Our refined values for the total moments on the Fe1 and Fe2 ions and for their direction cosines are listed in Table 4. At 10 K, our total moments on the Fe1 and Fe2 ions (4.16(4) and 4.20(3) μ_B, respectively) and for the direction cosines of the Fe1 moment with respect to the *a*, *b* and *c* axes (0.56(4), 0.31(7), 0.76(3)) are in

https://doi.org/10.1180/mgm.2023.66 Published online by Cambridge University Press

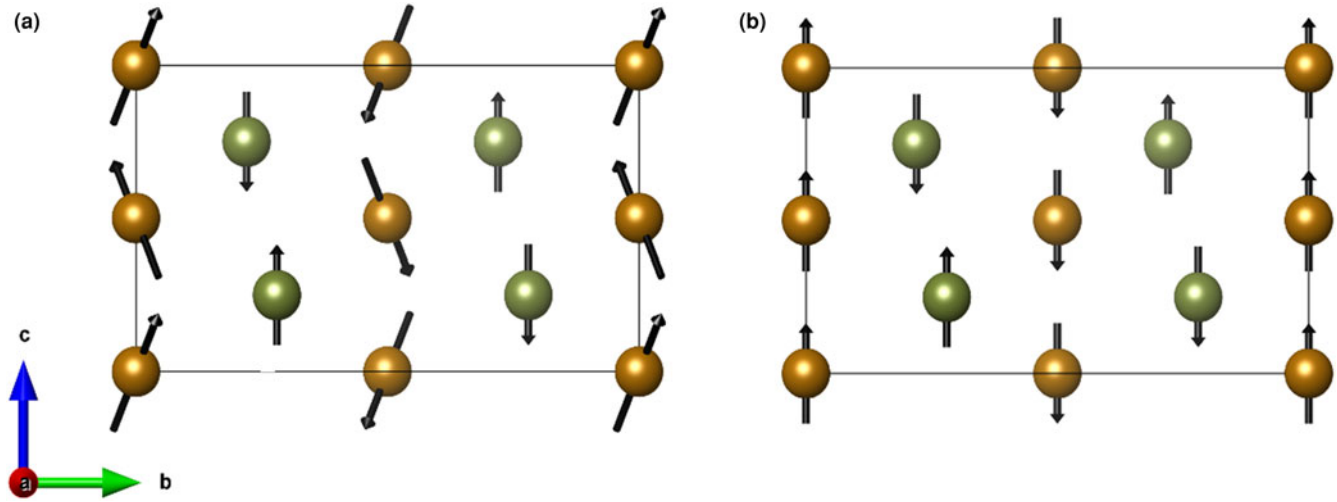

Figure. 7. Model of the spin configuration at: (a) 10 K in the canted and (b) at 40 K in the collinear antiferromagnetic regions. Fe1 ions (M1 sites) are shown in gold; Fe2 (M2) ions are shown in green.

Table 4. Fe_2SiO_4 Magnetic moments and direction cosines (numbers in parenthesis are one standard error of the least significant digits).

T (K)	Fe1 (μ_B)	cosα	cosβ	cosγ	Fe2 (μ_B)	cosγ
10	4.16(4)	0.56(4)	0.31(7)	0.76(3)	4.20(3)	1
15	3.94(9)	0.55(9)	0.29(4)	0.78(7)	4.16(7)	1
20	3.49(9)	0.52(10)	0.19(6)	0.83(7)	4.10(6)	1
25	2.93(6)	0	0	1	4.54(6)	1
30	2.69(7)	0	0	1	4.43(6)	1
35	2.43(7)	0	0	1	4.45(6)	1
40	2.37(5)	0	0	1	4.27(5)	1
45	2.25(8)	0	0	1	4.24(8)	1
50	2.15(9)	0	0	1	3.98(9)	1
55	1.87(10)	0	0	1	3.76(9)	1
60	1.56(13)	0	0	1	3.25(12)	1
65	0.90(20)	0	0	1	2.28(18)	1

very good agreement with the single-crystal results of Lottermoser *et al.* (1986), who found values of 4.41(5) and 4.4(1) μ_B, 0.57(2), 0.31(2) and 0.77(1). With increasing temperature, we find a gradual decline, more pronounced in the AFM2 phase, in the Fe1 magnetic moments, which are considerably reduced as compared both to the spin only value of $\mu = 4\ \mu_B$ and to those of the Fe2 site (Fig. 8). The behaviour of the moment on the Fe2 site is different, remaining fairly constant until ~50 K and then falling steeply. Once again, our results are in agreement with the trends observed by Müller *et al.* (1982) and Lottermoser *et al.* (1986).

Our results suggest that the Fe1 and Fe2 sites make separable and complementary contributions to the evolution of the lattice parameters of the AFM1 and AFM2 phases with temperature. The transition at 65.4 K from the paramagnetic state affects all axes, producing a decrease in *a* and *b*, but an increase in *c*; the

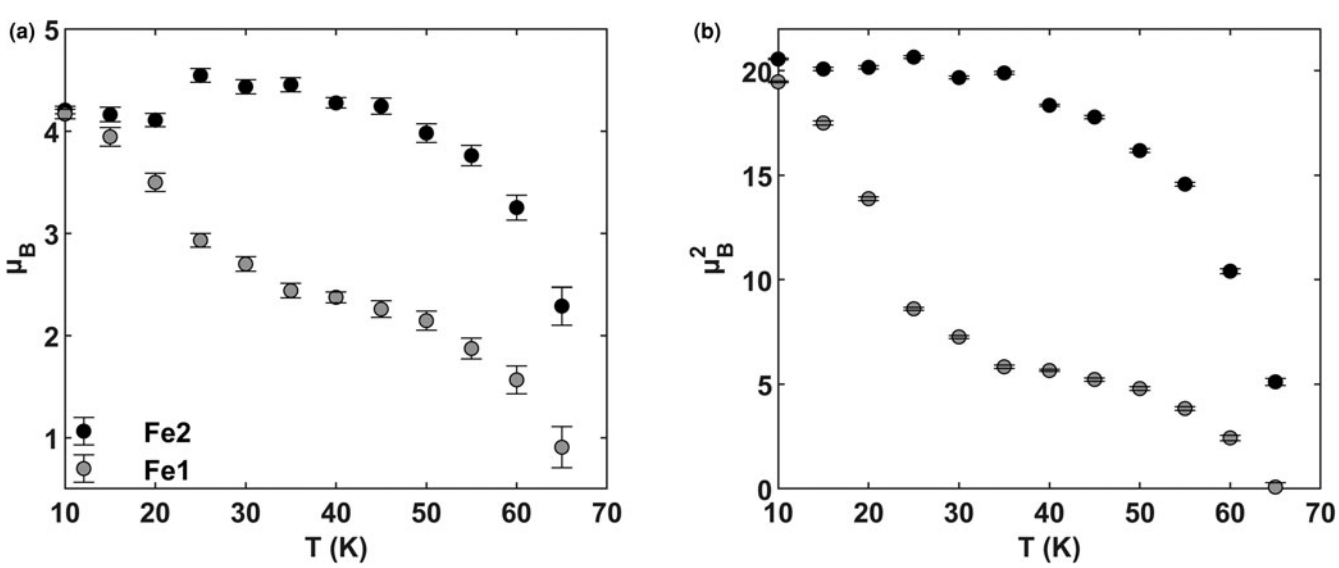

Figure 8. (a) Magnetic and (b) squared magnetic moments for the Fe1 (M1) and Fe2 (M2) sites as a function of temperature. Moments on the Fe1 site are considerably reduced as compared with Fe2 and the spin-only value of 4 μ_B (see Supplementary Table 1).

https://doi.org/10.1180/mgm.2023.66 Published online by Cambridge University Press

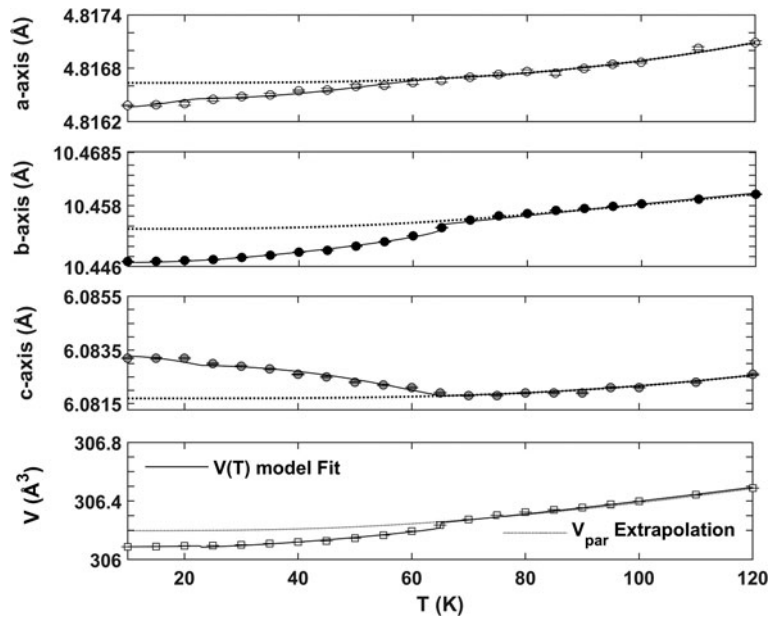

Figure 9. Lattice parameters of Fe_2SiO_4 below 120 K. Extrapolation of the paramagnetic behaviour of Fe_2SiO_4 below T_N using the 1st-order Grüneisen-Debye approximation of the thermal expansion (equation 4, with the parameter $b = 0$) is shown in dotted black lines and fitted magnetostrictive components (equation 7) in solid black lines.

effect of the transition at 23 K is much less pronounced, but is clearly visible in the *c* axis (Fig. 9). Changes in magnetic ordering in a crystal are, in general, accompanied by a magnetostrictive deformation. A method to obtain the spontaneous volume magnetostriction, ω_V, is to find the volume difference between the state in which the material is antiferromagnetically ordered, and a hypothetical state in which it is paramagnetically disordered (e.g. Kusz *et al.*, 2000).

$$\omega_V = \frac{V_{afm} - V_{par}}{V_{par}} \tag{11}$$

where V_{afm} and V_{par} are the antiferromagnetic (observed) and hypothetical paramagnetic values of the unit-cell volume below T_N, respectively. Similarly, the linear spontaneous magnetostriction can be calculated as

$$\lambda_X = \frac{X_{afm} - X_{par}}{X_{par}} \tag{12}$$

With X referring to the lattice parameters *a*, *b*, and *c*.

Clearly, the derived values of the spontaneous magnetostriction will be strongly dependent on the procedure used to extrapolate the cell parameters of the paramagnetic phase to temperatures below T_N. However, a further constraint on correctness is provided by the requirement that, for small strains,

$$\omega_V = \lambda_a + \lambda_b + \lambda_c \tag{13}$$

Initially, we determined the strains by fitting first-order Grüneisen approximations to the zero-pressure equation of state (e.g. Vočadlo *et al.*, 2002, equivalent to setting the parameter *b* in equation 4 to zero) to *a*, *b*, *c* and *V* in the range 70 K $\leq T \leq$ 200 K and then using these to extrapolate the paramagnetic behaviour into the AFM temperature range, but we then found that that the sum of the resulting axial magnetostrictive strains was not equal to the volumetric strain, as is required by equation 13. The reason for this is that the *b* axis varies essentially linearly for 65 K $\leq T \leq$ 200 K and so it cannot be reliably extrapolated in this way; the correlation coefficient between b_0 and θ_D in the non-linear least-squares algorithm was found to be 99.9%, and thus the temperature at which the thermal expansivity of the *b* axis begins to reduce, and hence its value at 0 K, cannot be determined. It was decided, therefore, that the most robust method for extrapolation of the cell parameters of the paramagnetic phase was to fit *a*, *c* and *V* in the range 70 K $\leq T \leq$ 200 K, as described above, and then to determine b_{par} from $V_{par}/(a_{par}c_{par})$. For $T \leq 65$ K, equation 7 was then fitted to the differences between the measured and the extrapolated cell parameters and the volumetric and linear magnetostrictive strains were calculated from equations 11 and 12 and were normalised to their calculated values at 0 K. The fitted lattice parameters are shown in Fig. 9, with the volumetric and linear spontaneous magnetostrictive strains given in Fig. 10a and the normalised magnetostrictive strains in Fig. 10b (the fitted values of the parameters are given in Supplementary Table 1; and Supplementary Fig. 2 shows the self-consistency of ω_V and $\lambda_a + \lambda_b + \lambda_c$). It can be seen from Fig. 10a that the strain λ_a is much smaller than λ_b and λ_c, for which the strains have opposite signs, and that the transition at 23 K has a minimal effect on the length of the *b* axis. In this latter respect, the behaviour of Fe_2SiO_4 at the 23 K transition is similar to that shown at the antiferromagnetic phase transition by Co_2SiO_4 (Sazonov *et al.*, 2010); however, in Co_2SiO_4, the values of λ_a and λ_c are in the opposite sense to those in Fe_2SiO_4. Comparison of the normalised values of the spontaneous magnetostriction (Fig. 10b) with the refined values of the magnetic moments on the Fe1 and Fe2 sites, Fig. 8, suggests that λ_a and λ_c show a temperature dependence that is similar to that of Fe1 moments whereas λ_b follows a trend more similar to that of the Fe2 sites.

Crystal structure

In Table 1, we present our refined values of the atomic coordinates for Fe_2SiO_4 for the 10 well-counted data sets spanning the

https://doi.org/10.1180/mgm.2023.66 Published online by Cambridge University Press

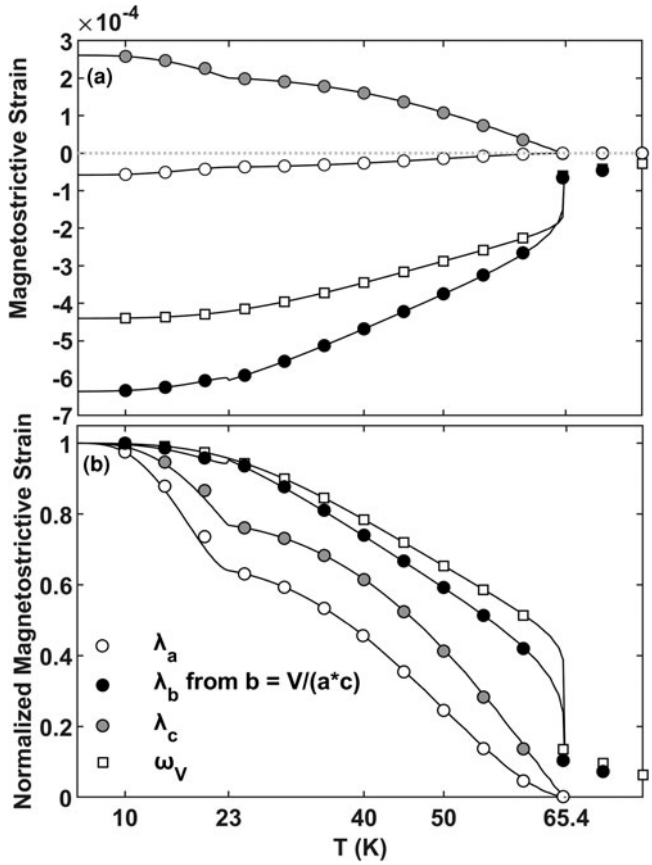

Figure 10. (a) Linear and volumetric spontaneous magnetostriction of Fe_2SiO_4. Experimental values (shown as symbols) were obtained from equation 11 and equation 12; the lines show the values calculated from equations 4 and 7 (for the volume) and 9 and 10 (for the axes). (b) Normalised values of spontaneous magnetostriction, with symbols as for (a), with the *a* and *c* axes showing a similar temperature dependence to that of Fe1 (M1) moments while *b* and *V* follow temperature dependences more like that of the moments on the Fe2 (M2) sites.

range from 10 K to 1453 K. However, as it was found that even the shorter counting times allowed us to obtain structure refinements of very good precision, the derived parameters characterising the $Fe1O_6$, $Fe2O_6$ and SiO_4 coordination polyhedra are shown in Fig. 11 and Fig. 12 for all data, with the numerical values listed in Supplementary Tables 2–5. None of the quantities plotted show any significant differences in behaviour associated with the onset of the paramagnetic ordering.

In Fe_2SiO_4 we find that the average Fe–O bond distances in both the $Fe1O_6$ and $Fe2O_6$ coordination octahedra show a roughly linear dependence on temperature, with Fe1–O increasing at ~6.36×10^{-4} Å K^{-1} and Fe2–O at ~7.53×10^{-4} Å K^{-1},while the shorter and more rigid Si–O bonds show very little, to no, expansion; the same features are visible in the volumes of the coordination polyhedra (Fig. 11). Various measures of the distortion of the polyhedra are shown in Fig. 12. The angular variance of the SiO_4 tetrahedra (defined as $\sum(\widehat{OSiO}-109.47)^2/6)$ is almost invariant, whereas the $Fe1O_6$ and $Fe2O_6$ octahedral angular variances (defined as $\sum(\widehat{OMO}-90)^2/12)$ both increase roughly linearly with temperature with a possible sharper increase above ~1300 K. Figure 12 also shows the polyhedral volume distortions from ideal polyhedra, as calculated by the program *Ivton2* (Balić-Žunić and Vicković, 1996). These were obtained via the relationship $(V_i - V_d)$ / V_i, where V_d is the volume of the measured coordination polyhedron and V_i the volume of the ideal polyhedron having fixed angles and an average for bond distances (taken from the centroid of the polyhedron to the coordinating ligands). The distortion of the SiO_4 tetrahedral sites remains almost constant throughout the temperature range. As was seen in the octahedral angular variances, the smaller $Fe1O_6$ octahedron remains more distorted throughout the temperature range and the distortion increases at a slightly faster rate (~1.4×10^{-4} K^{-1}) than that of the larger $Fe2O_6$ octahedron (~9.0×10^{-5} K^{-1}) in agreement with suggestions (e.g. Burns and Sung, 1978), that the larger thermal expansion of the *c* axis results from the tendency of the $Fe1O_6$ octahedra to elongate.

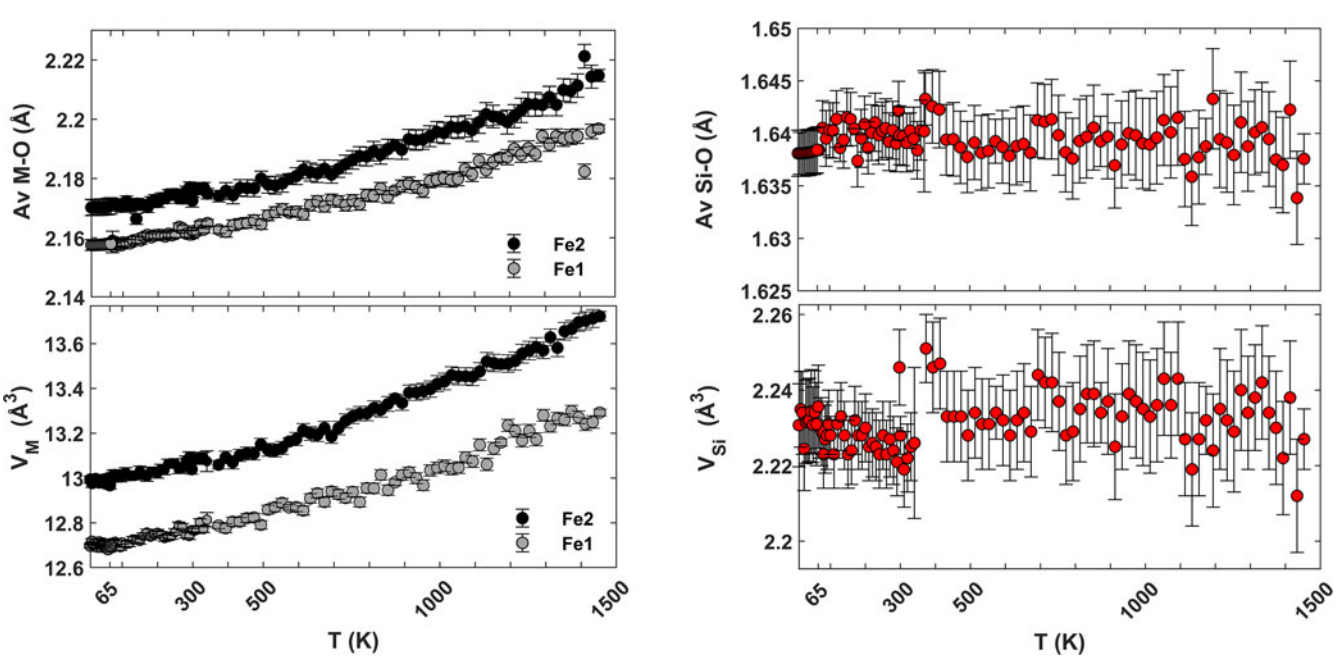

Figure 11. Fe_2SiO_4: Average polyhedral bond distances and polyhedral volumes as a function of temperature.

https://doi.org/10.1180/mgm.2023.66 Published online by Cambridge University Press

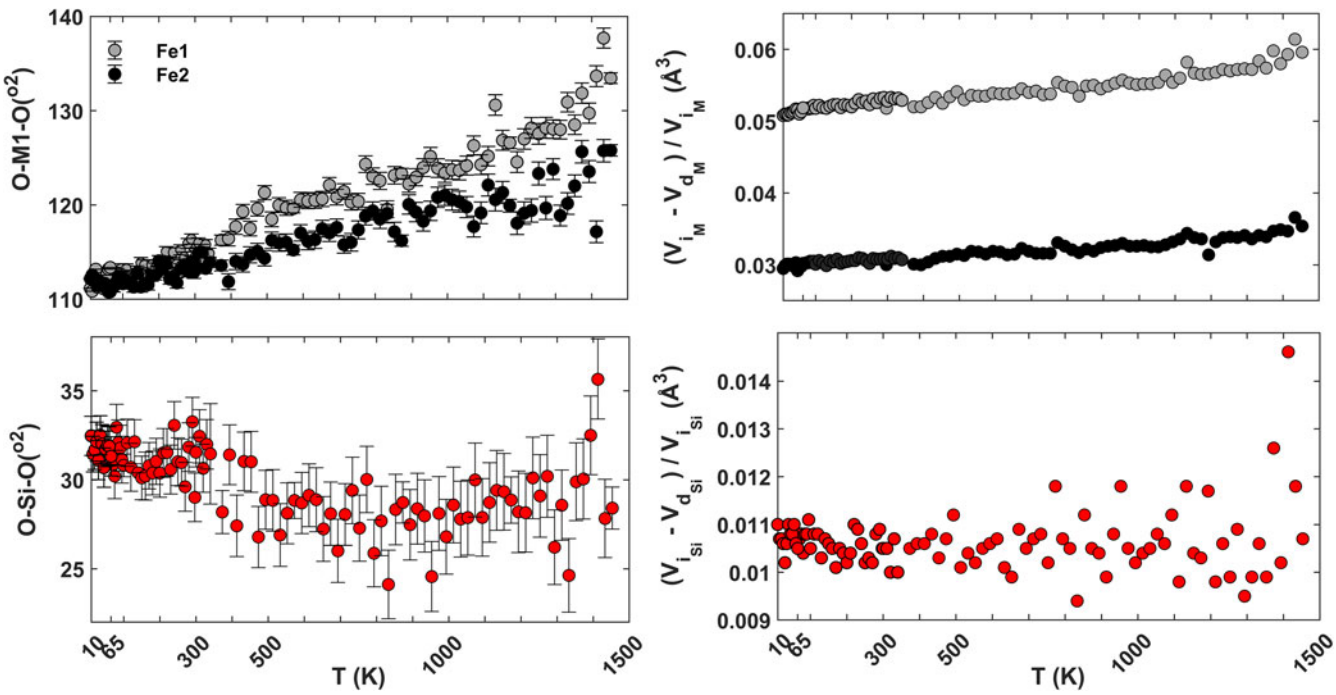

Figure 12. Fe_2SiO_4: Angular variances (left column) and volumetric distortions (right column) from the ideal polyhedra as a function of temperature.

Conclusions

We have collected high-resolution neutron powder diffraction patterns from Fe_2SiO_4 over the widest range of temperatures yet reported, from 10 K to 1453 K, which is within 25 K of the melting point (1478 K), at a homologous temperature of 0.983. Our refined lattice parameters are of substantially better accuracy and precision than any preceding diffraction study, allowing us to investigate the effect of the two antiferromagnetic transitions on the lattice parameters of Fe_2SiO_4 and thereby determine the spontaneous magnetostrictive strains. Our refinements of the magnetic structures confirm that the unit cell and space group (*Pbnm*) remain the same in all phases of Fe_2SiO_4. The moments on the Fe2 (M2) sites remain collinear and parallel to the *c* axis at all temperatures below 65.4 K. Below 65.4 K, the spins on the Fe1 (M1) sites are collinear and parallel to the *c* axis, but below 23 K, they become canted, possessing components along all three crystallographic directions.

The behaviour of the unit-cell volume of Fe_2SiO_4 is adequately described by a Grüneisen approximation to the zero-pressure equation of state, combined with a model of the magnetostriction based on modified mean-field curves, so as to include the contributions of the two AFM transitions at 23 K and 65.4 K. However, in the paramagnetic phase, the temperature dependence of the linear thermal expansion coefficient of the *b* axis takes an unusual form. In contrast to the unit-cell volume and to the *a* and *c* axes, for which the thermal expansion coefficients show the expected reduction in magnitude below ~300 K, the expansion coefficient of the *b* axis remains almost constant between ~70 K and 1000 K. This behaviour has been reported previously by e.g. Suzuki *et al.* (1981) above room temperature, but we have now shown that it persists to 70 K, i.e. throughout the paramagnetic phase field. Calculation of the average interatomic distances, and the volumes, angular variances, and distortions of the coordination polyhedra show that the changes with temperature in the FeO_6 and SiO_4 polyhedra are small, with the SiO_4 tetrahedra almost invariant. The volumes and distortions of the FeO_6 octahedra increase roughly linearly with temperature, with the smaller $Fe1O_6$ octahedron remaining more distorted throughout. In a future accompanying paper we intend to compare the thermal expansion coefficients of Fe_2SiO_4 with those of Mg_2SiO_4 and to discuss further the effects of temperature on the structures of these two olivine end-members.

Acknowledgements. We acknowledge the support of the Natural Environment Research Council, NERC, grants NE/S007229/1 and NE/T006617/1 and the ISIS Facility for the provision of beam-time (RB1910186, doi:10.5286/ISIS.E.RB1910186). The authors are grateful to the Pressure and Furnaces technicians who supported the high-temperature neutron diffraction measurements. The ISIS Design Division, in particular Ali Mortazavi, are thanked for the development of the new TZM sample can used for the first time as part of this study.

Supplementary material. The supplementary material for this article can be found at https://doi.org/10.1180/mgm.2023.66.

Competing interests. The authors declare none.

References

Anderson O.L. and Isaak D.G (1995) Elastic constants of mantle minerals at high temperature. Pp. 64–97 in: *AGU Reference Shelf 2: Mineral Physics and Crystallography: a Handbook of Physical Constants*. (T.J. Ahrens, editor) AGU, Washington.

Anderson O.L. and Suzuki I. (1983) Anharmonicity of three minerals at high temperature: forsterite fayalite and periclase. *Journal of Geophysical Research: Solid Earth*, **88**(B4), 3549–3556.

Angel R.J., Alvaro M. and Gonzalez-Platas J. (2014) EosFit7c and a Fortran module (library) for equation of state calculations. *Zeitschrift für Kristallographie-Crystalline Materials*, **229**, 405–419.

Arnold O., Bilheux J.C., Borreguero J.M., Buts A., Campbell S.I., Chapon L., Doucet M., Draper N., Leal R.F., Gigg M.A. and Lynch V.E. (2014)

Mantid—Data analysis and visualization package for neutron scattering and μ SR experiments. *Nuclear Instruments and Methods in Physics Research Section a: Accelerators, Spectrometers, Detectors and Associated Equipment*, **764**, 156–166.

Aronson M.C., Stixrude L., Davis M.K., Gannon W. and Ahilan K. (2007) Magnetic excitations and heat capacity of fayalite, Fe_2SiO_4. *American Mineralogist*, **92**, 481–490.

Balić-Žunić T. and Vicković I. (1996) IVTON: A program for the calculation of geometrical aspects of crystal structures and some crystal chemical applications. *Journal of Applied Crystallography*, **29**, 305–306.

Bass J.D. and Anderson D.L. (1984) Composition of the upper mantle: geophysical tests of two petrological models. *Geophysical Research Letters*, **11**, 237–240.

Béjina F., Bystricky M., Tercé N., Whitaker M.L. and Chen H. (2019) Bulk modulus of Fe-rich olivines corrected for non-hydrostaticity. *Comptes Rendus Geoscience*, **351**, 86–94.

Béjina F., Bystricky M., Tercé N., Whitaker M.L. and Chen H. (2021) Equation of state and sound wave velocities of fayalite at high pressures and temperatures: implications for the seismic properties of the Martian mantle. *European Journal of Mineralogy*, **33**, 519–535.

Blundell S. (2001) *Magnetism in Condensed Matter*. Oxford University Press, UK.

Bragg W.L. and Brown G.B. (1926) XXX. Die Struktur des Olivins. Zeitschrift für Kristallographie-*Crystalline Materials*, **63**, 538–556.

Burns R.G. and Sung C.M. (1978) The effect of crystal field stabilization on the olivine to spinel transition in the system Mg_2SiO_4–Fe_2SiO_4. *Physics and Chemistry of Minerals*, **2**, 349–364

Cochran W. (1973) *The Dynamics of Atoms in Crystals*. E. Arnold, London

Cococcioni M., Dal Corso A. and de Gironcoli S. (2003) Structural, electronic, and magnetic properties of Fe_2SiO_4 fayalite: Comparison of LDA and GGA results. *Physical Review B*, **67**, 094106.

Cox D.E., Frazer, B.C., Almodovar, I. and Kay, M.I. (1965) The magnetic structures of Fe_2SiO_4 and Mn_2SiO_4. *Abstracts of the American Crystallographic Association Annual Meeting*, Gatlinburg, Tennessee, USA.

Dekker A.J. (1964) *Solid State Physics*. Macmillan, London.

Dobson D.P. (2021) The tungsten carbide–carbon monoxide–tungsten buffer and its use for synthesizing iron-bearing silicates in muffle furnaces. *Review of Scientific Instruments*, **92**, 055101.

Ehrenberg H. and Fuess H. (1993) Analytical interpretation and simulation of the static magnetic properties of synthetic alpha-Fe_2SiO_4. *Journal of Physics: Condensed Matter*, **5**, 3663.

Fei Y. (1995) Thermal Expansion. Pp. 29–44 in: *AGU Reference Shelf 2: Mineral Physics and Crystallography: a Handbook of Physical Constants*. (T.J. Ahrens, editor) AGU, Washington.

Fortes A.D. (2019) Thermal expansion of the Al_2SiO_5 polymorphs, kyanite, andalusite and sillimanite, between 10 and 1573 K determined using time-of-flight neutron powder diffraction. *Physics and Chemistry of Minerals*, **46**, 687–704.

Fuess H., Ballet O. and Lottermoser W. (1988) Magnetic phase transition in olivines M_2SiO_4 (M = Mn, Fe, Co, Fe_xMn_{1-x}) Pp. 185–207 in: *Structural and Magnetic Phase Transitions in Minerals* (S. Ghose, J.M.D. Coey and E. Salje, editors). Springer, Berlin.

Graham E.K., Schwab J.A., Sopkin S.M. and Takei H. (1988) The pressure and temperature dependence of the elastic properties of single-crystal fayalite Fe_2SiO_4. *Physics and Chemistry of Minerals*, **16**, 186–198.

Hafner S.S., Stanek J. and Stanek M. (1990) ^{57}Fe Hyperfine interactions in the magnetic phase of fayalite, Fe_2SiO_4. *Journal of Physics and Chemistry of Solids*, **51**, 203–208.

Hazen R.M. (1977) Effects of temperature and pressure on the crystal structure of ferromagnesian olivine. *American Mineralogist*, **62**, 286–295.

Hunt S.A., Wann E.T., Dobson D.P., Vočadlo L. and Wood I.G. (2017) The thermal expansion of $(Fe_{1-y}Ni_y)Si$. *Journal of Physics: Condensed Matter*, **29**, 335701.

Ibberson R.M. (2009) Design and performance of the new supermirror guide on HRPD at ISIS. *Nuclear Instruments and Methods in Physics Research Section A: Accelerators, Spectrometers, Detectors and Associated Equipment*, **600**, 47–49.

Ibberson R.M., David W.I.F. and Knight K.S. (1992) *Report RAL–92–031*. Rutherford Appleton Laboratory, UK.

Kondo H. and Miyahara S. (1963) Magnetic properties of some synthetic olivines. *Journal of the Physical Society of Japan*, **18**, 305.

Kozu S., Ueda J.I. and Tsurumi S. (1934) Thermal expansion of olivine. *Proceedings of the Imperial Academy*, **10**, 83–86.

Kroll H., Kirfel A., Heinemann R. and Barbier, B. (2012) Volume thermal expansion and related thermophysical parameters in the Mg, Fe olivine solid-solution series. *European Journal of Mineralogy*, **24**, 935–956.

Kroll H., Kirfel A. and Heinemann R. (2014) Axial thermal expansion and related thermophysical parameters in the Mg, Fe olivine solid-solution series. *European Journal of Mineralogy*, **26**, 607–621.

Kusz J., Böhm H. and Talik E. (2000) X-ray investigation and discussion of the magnetostriction of Gd_3T (T= Ni, Rh, Irx) single crystals. *Journal of Applied Crystallography*, **33**, 213–217.

Larson A. and Von Dreele R. (2000) *General Structure Analysis System (GSAS)*. Report LAUR 86–748. Los Alamos National Laboratory, New Mexico, USA.

Lindsay-Scott A., Wood I.G. and Dobson D.P. (2007) Thermal expansion of $CaIrO_3$ determined by X-ray powder diffraction. *Physics of the Earth and Planetary Interiors*, **162**, 140–148.

Lottermoser W., Müller R. and Fuess H. (1986) Antiferromagnetism in synthetic olivines. *Journal of Magnetism and Magnetic Materials*, **54**, 1005–1006.

Lottermoser W., Forcher K., Amthauer G. and Fuess H. (1995) Powder-and single crystal Mössbauer spectroscopy on synthetic fayalite. *Physics and Chemistry of Minerals*, **22**, 259–267.

Lottermoser W., Forcher K., Amthauer G., Treutmann W. and Hosoya S. (1996) Single crystal Mössbauer spectroscopy on the three principal sections of a synthetic fayalite sample in the antiferromagnetic state. *Physics and Chemistry of Minerals*, **23**, 432–438.

Mantid (2013) *Mantid Project*. https://doi.org/10.5286/SOFTWARE/MANTID

Momma K. and Izumi F. (2011) VESTA 3 for three-dimensional visualization of crystal, volumetric and morphology data. *Journal of Applied Crystallography*, **44**, 1272–1276.

Müller R., Fuess H. and Brown P.J. (1982) Magnetic properties of synthetic fayalite (α-Fe_2SiO_4). *Le Journal de Physique Colloques*, **43**(C7), C7–249.

Rigby G.R., Lovell G.H.B. and Green A.T. (1946) The reversible thermal expansion and other properties of some magnesian ferrous silicates. *Transactions of the British Ceramic Society*, **44**, 237–250.

Ringwood A.E. (1969) Phase transformations in the mantle. *Earth and Planetary Science Letters*, **5**, 401–412.

Santoro R.P., Newnham R.E. and Nomura S. (1966) Magnetic properties of Mn_2SiO_4 and Fe_2SiO_4. *Journal of Physics and Chemistry of Solids*, **27**, 655–666.

Sazonov A., Hutanu V., Meven M., Heger G., Hansen T. and Senyshyn A. (2010) Anomalous thermal expansion of cobalt olivine, Co_2SiO_4, at low temperatures. *Journal of Applied Crystallography*, **43**, 720–728.

Simmons R.O. and Balluffi R.W. (1962) Measurement of equilibrium concentrations of lattice vacancies in gold. *Physical Review*, **125**, 862–872.

Skinner B.J. (1962) Thermal expansion of ten minerals. *U.S. Geological Survey Professional Paper*, **450**, l09–l12.

Speziale S., Duffy T.S. and Angel R.J. (2004) Single-crystal elasticity of fayalite to 12 GPa. *Journal of Geophysical Research: Solid Earth*, **109**, B12202.

Sumino Y. (1979) The elastic constants of Mn_2SiO_4, Fe_2SiO_4 and Co_2SiO_4, and the elastic properties of olivine group minerals at high temperature. *Journal of Physics of the Earth*, **27**, 209–238.

Suzuki I., Seya K., Takei H. and Sumino Y. (1981) Thermal expansion of fayalite, Fe_2SiO_4. *Physics and Chemistry of Minerals*, **7**, 60–63.

Toby B.H. (2001) EXPGUI, a graphical user interface for GSAS. *Journal of Applied Crystallography*. **34**, 210–213.

Vočadlo L., Knight K.S., Price G.D. and Wood I.G. (2002) Thermal expansion and crystal structure of FeSi between 4 and 1173 K determined by time-of-flight neutron powder diffraction. *Physics and Chemistry of Minerals*, **29**, 132–139.

Wallace D.C. (1998) *Thermodynamics of Crystals*. Dover, New York.

Wood I.G., Knight K.S., Price G.D. and Stuart J.A. (2002) Thermal expansion and atomic displacement parameters of cubic $KMgF_3$ perovskite determined by high-resolution neutron powder diffraction. *Journal of Applied Crystallography*, **35**, 291–295.

https://doi.org/10.1180/mgm.2023.66 Published online by Cambridge University Press

Wood I.G., Vočadlo L., Knight K.S., Dobson D.P., Marshall W.G., Price G.D. and Brodholt J. (2004) Thermal expansion and crystal structure of cementite, Fe_3C, between 4 and 600 K determined by time-of-flight neutron powder diffraction. *Journal of Applied Crystallography*, **37**, 82–90.

Zhang L. (1998) Single crystal hydrostatic compression of (Mg,Mn,Fe,Co)$_2SiO_4$ olivines. *Physics and Chemistry of Minerals*, **25**, 308–312.

Zhang J.S., Hu Y., Shelton H., Kung J. and Dera P. (2017) Single-crystal X-ray diffraction study of Fe_2SiO_4 fayalite up to 31 GPa. *Physics and Chemistry of Minerals*, **44**, 171–179.

https://doi.org/10.1180/mgm.2023.66 Published online by Cambridge University Press